Modelling point spread function in fluorescence microscopy with a sparse Gaussian mixture: trade-off between accuracy and efficiency

Denis K. Samuylov, Prateek Purwar, Gábor Székely, and Grégory Paul

Abstract—Deblurring is a fundamental inverse problem in bioimaging. It requires modelling the point spread function (PSF), which captures the optical distortions entailed by the image formation process. The PSF limits the spatial resolution attainable for a given microscope. However, recent applications require a higher resolution, and have prompted the development of super-resolution techniques to achieve sub-pixel accuracy. This requirement restricts the class of suitable PSF models to analog ones. In addition, deblurring is computationally intensive, hence further requiring computationally efficient models. A custom candidate fitting both requirements is the Gaussian model. However, this model cannot capture the rich tail structures found in both theoretical and empirical PSFs. In this paper, we aim at improving the reconstruction accuracy beyond the Gaussian model, while preserving its computational efficiency. We introduce a new class of analog PSF models based on Gaussian mixtures. The number of Gaussian kernels controls both the *modelling accuracy* and the *computational efficiency* of the model: the lower the number of kernels, the lower accuracy and the higher efficiency. To explore the accuracy–efficiency trade-off, we propose a variational formulation of the PSF calibration problem, where a convex sparsity-inducing penalty on the number of Gaussian kernels allows trading accuracy for efficiency. We derive an efficient algorithm based on a fully-split formulation of alternating split Bregman. We assess our framework on synthetic and real data and demonstrate a better reconstruction accuracy in both geometry and photometry in point source localisation—a fundamental inverse problem in fluorescence microscopy.

Index Terms—Quantitative fluorescence microscopy, model-based image processing, Bayesian modelling, alternating split Bregman, point spread function, parametric dictionary, virtual microscope framework

I. INTRODUCTION

INCOHERENT imaging systems are linear in power (*i.e.* intensity) and are well described by linear system theory: the mean intensity image results from the *superposition integral* of the true object intensity weighted by the *point spread function* (PSF). The PSF encodes the propagation of the incoherent light emitted by a unit-intensity point source object through the optics up to the array of photo-detectors. In turn, the mean intensity parameterises the statistical model that accounts for the intrinsic stochastic nature of light emission (see *e.g.* [1], [2], [3]). Together with other sources of distortion, this defines the image formation process, *i.e.* the *forward problem*.

Solving the *inverse problem* for an incoherent imaging system amounts to reconstructing the number (amount), the position (geometry), and the intensity (photometry) of the emitting light sources. Depending on the nature of the reconstruction

space, *digital* or *analog*, the task is qualitatively different. In the digital case, the number and position of the light sources in physical space are lost: only the integrated intensity at each pixel position is reconstructed. On the contrary, an analog reconstruction aims at resolving the number, the position, and the intensity of the emitting light sources *in physical space*. The PSF and the inherent noise in the acquisition process make this inverse problem ill-posed and ill-conditioned. Therefore, "good" models about the forward problem and the imaged objects are necessary for solving this problem. In this work, we focus on modelling the first step of the image formation process by finding a PSF representation, suitable for solving imaging inverse problems in an *analog reconstruction space*.

The quality of the PSF model determines the accuracy of the imaged object reconstruction, thus its knowledge is fundamental for solving bio-imaging inverse problems [4], [5], [6]. One approach is to assume that the PSF is unknown and to include its estimation in the inverse problem (blind deconvolution, see *e.g.* [7], [8]). However, it makes the problem more ill-conditioned. Therefore, we focus on estimating the PSF as a separate task. We also restrict ourselves to shift-invariant imaging systems, excluding space-varying PSF models.

PSF models can be classified according to different criteria: *model-based vs. phenomenological*, *digital vs. analog*, and *calibrated vs. uncalibrated*. The PSF model can be derived either from modelling the imaging systems or from imaging point-like objects. A digital PSF is well-suited for a digital reconstruction space, but not adapted to analog reconstructions; whereas an analog PSF can be used both in analog and digital reconstructions (after appropriate integration and sampling). Finally, if the PSF model is calibrated experimentally on a specific imaging system, we call this PSF *calibrated*. These criteria define a range of possible models. At the two extremes stand the theoretical (derived from optics) and the empirical (punctual source measurements) PSF models. The former is analog and can potentially achieve sub-pixel resolution, but at the expense of costly convolution algorithms. On the contrary, the latter is digital and therefore amenable to efficient convolution algorithms (based on the fast Fourier transform, FFT), but at the expense of a loss in accuracy.

Theoretical PSF models are derived from modelling the microscope optics. Their differences lie in their level of simplification. The simplest models use the paraxial approximation, which is valid for objectives with a small numerical aperture (NA), thin imaged specimens, and ideal acquisition conditions [9]. More advanced models account for the spherical aberra-

tions due to sample thickness and refractive indexes mismatch [10]. Recent models use the vectorial theory of diffraction to extend PSF models to objectives with a high NA [11], [12], [13], [14]. In practice, this class of PSF models is difficult to use because hard or impossible to calibrate (*e.g.* unknown refractive index of the immersion medium [6]). In addition, a specific imaging system can deviate from these idealised models in at least two ways (*e.g.* [10], [15]): the experimental setup does not fit the model assumptions or variations in the optics (*e.g.* lens imperfections, optics misalignment) create distortions not accounted for by the models.

Empirical PSF models are derived from *calibration data*, namely an image stack of point-like objects, such as quantum dots, fluorescent beads (*e.g.* [16], [17], [18], [19], [20]) or small structures within the sample [21]. Calibration data provide an accurate representation of the PSF only for specific imaging conditions [16]. Any deviation from the expected PSF image can be used to identify problems in the experimental setup (*e.g.* oil mismatch, vibrations from the heating system [15], [20]). However, it also imposes a restriction: calibration data must be acquired under the same conditions as the specimen, *i.e.* from point-like objects embedded within the sample [5], [15]. This is rarely feasible in practice and may require advanced measurement techniques [22]. Moreover, empirical PSF models require correcting the corruptions entailed by the image formation process, *e.g.* by removing the background signal, denoising, or accounting for the extended geometry of point-like objects (*e.g.* [23], [4], [15], [24]).

The two ends of the spectrum of possible PSF models illustrate a trade-off between accuracy and efficiency. On one end, theoretical PSF models can be used to resolve the localisation of individual point sources in physical space, at the expense of robustness (difficulty to fit a specific setup) and computational efficiency (analog PSF are typically more expensive to evaluate than digital ones). On the other end, digital PSF models are computationally efficient to use (*e.g.* thanks to fast algorithms such as FFT), but their resolution is limited by the pixel grid. Between these two extremes, one can trade accuracy for efficiency or *vice versa*. For example, theoretical PSF models can be adjusted to a specific setup by using PSF measurements (*e.g.* [6], [25], [24]). This improves robustness, but does not solve the computational efficiency problem. For this purpose, a well-spread solution is to use a Gaussian PSF model approximating the real PSF of a specific imaging system (*e.g.* [26]). Such models are well suited for modelling the in-focus section of the PSF [27], but results in a poor approximation of the PSF tails [28] and are not suitable for modelling the 3D PSF of a widefield microscope [26]. In order to explore the trade-off between accuracy and efficiency, a solution is to use *analog phenomenological models*. These models are flexible enough to accommodate real PSF shapes, and still computationally efficient. Moreover, their complexity can be adjusted according to the desired trade-off between accuracy and efficiency. For example, Zernike moments can encode reflection-symmetric PSFs [29], [30] with a complexity controlled by the number of moments used in the model. More recently, polynomial B-splines were proposed [31], [32]. In that case, the trade-off can be explored by varying the

number and placement of the basis functions. Nonetheless, to the best of our knowledge, this trade-off has not yet been systematically explored in the literature.

In this paper, we aim at improving the PSF reconstruction accuracy beyond single Gaussian models that misapproximates the PSF tails [28]. Therefore, we propose a new class of phenomenological PSF models with an adjustable level of complexity that can be tuned to achieve a desired accuracy–efficiency trade-off. We model the PSF as a sparse mixture of multivariate Gaussian distributions. The motivation behind this choice is a fast algorithm to compute non-gridded convolutions with Gaussian kernels: the improved fast Gaussian transform (IFGT, [33]).

II. FORWARD PROBLEM

To ease the reading of the presentation of the forward problem we provide in Table V a summary of the notations used in the forthcoming sections in the appendix.

A. Object model

We assume that the PSF measurements result from imaging a fluorescent bead with a size below the resolution limit of the microscope objective, thus approximating an idealised *point source* (PS) object [15]. We further assume that during acquisition, the fluorescent bead is immobile and emits photons at a constant rate (*i.e.* we neglect photo-bleaching). The total photon flux decomposes as the contribution of the photons emitted by the PS located at $\boldsymbol{x}^{\mathrm{ps}} \in \mathbb{R}^3$ at rate $\varphi^{\mathrm{ps}} \in \mathbb{R}_+$ and the photons emitted by the background (due to autofluorescence) at a constant rate $\varphi^{\mathrm{bg}} \in \mathbb{R}_+$. We use the measure-theoretical framework of [34] to model the total photon flux as a spatio-temporal object measure:

$$\phi^{\mathrm{obj}}(\mathrm{d}\boldsymbol{y} \times \mathrm{d}t) = \left(\varphi^{\mathrm{ps}}\delta_{\boldsymbol{x}^{\mathrm{ps}}}(\mathrm{d}\boldsymbol{y}) + \varphi^{\mathrm{bg}}\,\mathrm{d}\boldsymbol{y}\right)\mathrm{d}t \ . \quad (1)$$

B. Image formation process

The image formation in fluorescence microscopy can be modelled as a two-stage process [34], [1]. The *object-to-pixel mapping* models the optical distortions due to the random nature of light emission and propagation: it integrates the expected photon flux emitted by a set of fluorescent objects located in physical space over the pixel surface during the exposure time and models the number of photons hitting each photo-detector. The *pixel-to-image mapping* models the conversion of photon counts collected at each pixel to image grey values and accounts for the measurement noise, *e.g.* due to the photoelectric effect, signal amplification, noise in the electronic circuitry and quantisation [35], [36].

1) Object-to-pixel mapping: The PSF tails are in the low-intensity region where the fluctuations inherent to light emission are measurable and photon shot-noise is significant. Therefore, we use a Poissonian model for the photon counting statistics. We denote the imaging volume as $\Omega \subset \mathbb{R}^3$ and model the photon count at pixel $\mathcal{P}_j \subset \Omega$ during the exposure time t_e as a random variable N_j^{photon} following a Poisson distribution with mean intensity μ_j:

$$N_j^{\mathrm{photon}} \sim \mathrm{Poisson}(\mu_j) \ . \quad (2)$$

(a) Synthetic Born and Wolf   (b) Widefied fluorescence microscopy   (c) Laser scanning confocal microscopy
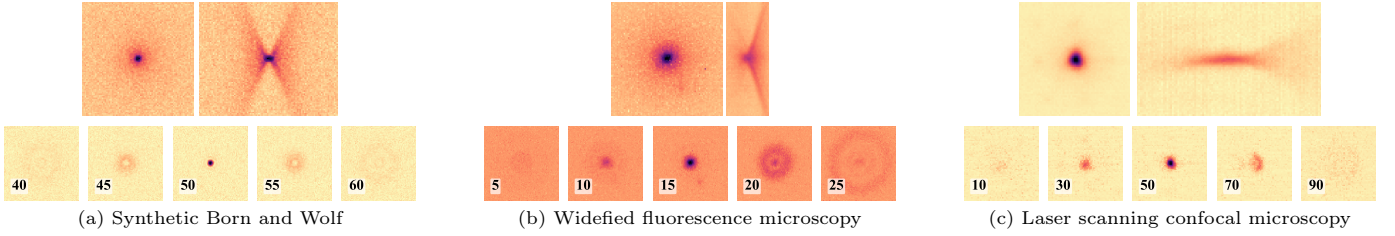
Figure 1. **Fluorescent bead image data for different imaging modalities.** (a) Synthetic image stack of an idealised PS object using the forward model in Section II and the BW PSF model. (b)-(c) Real image data of nanoscale beads acquired using a *widefied fluorescence microscopy* (b) and a *laser scanning confocal microscopy* (c). Orthogonal z- and x- mean projections (*first row*) and sample focal planes (*second row*) shown in log-colour scale.

In incoherent imaging, the mean intensity at a given location in the image plane results from the superposition of the independent contributions of the light sources distributed in physical space. For each individual light source, the photon flux observed under a specific imaging system is entirely characterised by the PSF. After a proper normalisation, the PSF can be understood microscopically as the transition probability kernel, denoted $\kappa(\mathrm{d}\boldsymbol{x} \mid \boldsymbol{y})$, translating individual photons in the image plane around $\mathrm{d}\boldsymbol{x}$, conditionally on the position $\boldsymbol{y}$ of the emitting light source [37], [1], [38].

For a general object modelled as a spatio-temporal measure, denoted ϕ, the expected photon count at j-th pixel is described as a superposition integral:

$$\mu_j(\phi) = \int_{\mathcal{P}_j \times [0, t_e]} \int_\Omega \kappa(\mathrm{d}\boldsymbol{x} \mid \boldsymbol{y}) \, \phi(\mathrm{d}\boldsymbol{y} \times \mathrm{d}t) \ . \qquad (3)$$

We assume that the imaging setup is well described by a shift-invariant PSF. In this case, the superposition integral becomes a convolution integral:

$$\int_\Omega \kappa(\mathrm{d}\boldsymbol{x} \mid \boldsymbol{y}) \, \phi(\mathrm{d}\boldsymbol{y} \times \mathrm{d}t) = (\kappa * \phi)(\mathrm{d}\boldsymbol{x} \times \mathrm{d}t) \ . \qquad (4)$$

For a set of PSs with position and intensity $\{(\boldsymbol{x}_s, \varphi_s)\}_s$, equation (4) transforms in a linear combination of shifted PSF:

$$\left(\kappa * \sum_s \varphi_s \delta_{\boldsymbol{x}_s} \right)(\mathrm{d}\boldsymbol{x} \times \mathrm{d}t) = \left(\sum_s \varphi_s \kappa(\boldsymbol{x} - \boldsymbol{x}_s) \right) \mathrm{d}\boldsymbol{x} \, \mathrm{d}t \ .$$

We specialise the above equation to the object model (1) and use a mid-point quadrature to approximate the photon flux (3):

$$\mu_j(\phi) \approx \mu_j(\boldsymbol{x}^{\mathrm{ps}}, \varphi^{\mathrm{ps}}) := c \left(\varphi^{\mathrm{ps}} \kappa(\boldsymbol{x}_j - \boldsymbol{x}^{\mathrm{ps}}) + \varphi^{\mathrm{bg}} \right) \ , \quad (5)$$

where $\boldsymbol{x}_j \in \Omega$ is the centre of the j-th pixel, $c := |\mathcal{P}| t_e$ the spatio-temporal integration volume, and $|\mathcal{P}|$ the pixel area. For clarity we have omitted the dependence on φ^{bg}, that is estimated independently in practice. From now on, we rescale the photon emission rates by c to obtain the integrated intensities, that we denote for simplicity with the same symbols: $\varphi^{\mathrm{ps}} := c\varphi^{\mathrm{ps}}$ and $\varphi^{\mathrm{bg}} := c\varphi^{\mathrm{bg}}$. We assume that the pixels are back-projected onto the object space, *i.e.* the lateral pixel coordinates are divided by the magnification factor and the axial coordinate is aligned with the object [27].

2) Pixel-to-image mapping: Modelling the conversion of photons hitting the detector surface into grey values depends on the type of camera [35], [36]. We model the conversion by a deterministic affine mapping, denoted ν:

$$N_j^{\mathrm{grey}} = q_\lambda \, M \, f^{-1} N_j^{\mathrm{photon}} + b =: \nu(N_j^{\mathrm{photon}}) \ , \qquad (6)$$

where q_λ is the quantum efficiency at emission wavelength λ, M is the multiplication gain, f is the analog-to-digital proportionality factor, and b is the camera bias.

C. PSF models

We introduce three PSF models spanning the complexity range. The classical Born and Wolf (BW) model is used as a reference idealised model, assuming that the microscope is operated under design conditions. The single Gaussian (SG) model is a widespread PSF approximation because of its computational advantages. The Gaussian mixture (GM) model, which we propose in this work, represents a whole class of models that will allow us exploring the accuracy–efficiency trade-off. Each model is parameterised by a set of parameters, generically denoted $\boldsymbol{\theta}$, belonging to a set of admissible values, denoted $\boldsymbol{\Theta}$. When ambiguous, we will add a superscript to $\boldsymbol{\theta}$ and $\boldsymbol{\Theta}$ with the PSF model name. We denote by $\boldsymbol{x} := (x, y, z) \in \mathbb{R}^3$ an arbitrary point in physical space.

1) Born and Wolf (BW) model: The model is parameterised by three parameters, *i.e.* the emission wavelength, the numerical aperture, and the refractive index of the immersion medium, denoted $\boldsymbol{\theta}^{\mathrm{bw}} := \{\lambda, \mathrm{NA}, n_i\} \in \boldsymbol{\Theta}^{\mathrm{bw}} := \mathbb{R}_+^3$. The BW PSF kernel writes as:

$$\kappa_{\boldsymbol{\theta}}^{\mathrm{bw}}(\boldsymbol{x}) := C_{\boldsymbol{\theta}}^{\mathrm{bw}} \left| \int_0^1 J_0(k_0 \, r \, \mathrm{NA} \, \rho) \, \mathrm{e}^{-i \, \Phi(\rho, z)} \rho \, \mathrm{d}\rho \right|^2 \ ,$$

where $C_{\boldsymbol{\theta}}^{\mathrm{bw}}$ is the normalisation constant, J_0 denotes the Bessel function of the first kind of order zero, $\Phi(\rho, z) = \frac{k_0 z \mathrm{NA}^2 \rho^2}{2n_i}$ is the phase term, $k_0 = \frac{2\pi}{\lambda n_i}$ is the wavenumber in vacuum, and $r = \sqrt{x^2 + y^2}$.

2) Single Gaussian (SG) model: The SG model is simply a Gaussian density, with a particular covariance matrix: this model is radially symmetric around the z-axis. Therefore, it is parameterised by the lateral and axial standard deviations, denoted $\boldsymbol{\theta}^{\mathrm{sg}} := (\sigma_{xy}, \sigma_z) \in \boldsymbol{\Theta}^{\mathrm{sg}} \subset \mathbb{R}_+^2$. The SG PSF kernel is defined as $\kappa_{\boldsymbol{\theta}}^{\mathrm{sg}}(\boldsymbol{x}) = C_{\boldsymbol{\theta}}^{\mathrm{sg}} \mathrm{e}^{-\frac{1}{2}\boldsymbol{x}^T \Sigma_{\boldsymbol{\theta}}^{-1} \boldsymbol{x}}$, where $\Sigma_{\boldsymbol{\theta}} := \mathrm{diag}(\sigma_{xy}^2, \sigma_{xy}^2, \sigma_z^2) \in \mathbb{R}^{3 \times 3}$ is the covariance matrix. The normalisation constant is given by $C_{\boldsymbol{\theta}}^{\mathrm{sg}} = (8\pi^3 \sigma_{xy}^4 \sigma_z^2)^{-0.5}$.

3) Gaussian mixture (GM) model:

a) Definition: To explore the accuracy–efficiency trade-off, we introduce a Gaussian mixture model, namely a convex combination of Gaussian kernels shifted to different positions. The general GM model is described by a *parametric dictionary*, denoted $\mathcal{D}$, where each atom is a shifted SG kernel: $\mathcal{D} := \bigcup_{(\boldsymbol{\theta}_a, \boldsymbol{x}_a) \in \boldsymbol{\theta}^{\mathcal{D}}} \kappa_{\boldsymbol{\theta}_a}^{\mathrm{sg}}(\cdot - \boldsymbol{x}_a)$. However, in this paper we structure $\boldsymbol{\theta}^{\mathcal{D}}$ by a set of n^{c} covariance matrices: for each $\boldsymbol{\theta}_k^{\mathrm{sg}}$ with $\mathcal{K} := \{1, \ldots, n^{c}\}$ we associate a set of positions, defined as $\mathcal{X}_k := \bigcup_{m \in \mathcal{M}_k} \boldsymbol{x}_{km}$ with $\mathcal{M}_k := \{1, \ldots, n_k^{\mathcal{X}}\}$: $\boldsymbol{\theta}^{\mathcal{D}} := \bigcup_{k \in \mathcal{K}} \{\boldsymbol{\theta}_k^{\mathrm{sg}}\} \times \mathcal{X}_k =: \bigcup_{k \in \mathcal{K}} \boldsymbol{\theta}_k^{\mathcal{D}}$. The dictionary size corresponds to the number of Gaussian kernels in the mixture, defined as $|\mathcal{D}| = \sum_{k \in \mathcal{K}} n_k^{\mathcal{X}}$. To ensure the proper normalization of the PSF, a GM model is defined as a *convex combination* of the Gaussian kernels in the dictionary $\mathcal{D}$. The mixture weight vector is denoted $\boldsymbol{v}$ and belongs to the $|\mathcal{D}|$-simplex, denoted $\Delta_{|\mathcal{D}|}$, *i.e.* $\boldsymbol{v}$ must have positive components summing to one. The parameters are the dictionary parameters and the mixture weights vector, *i.e.* $\boldsymbol{\theta}^{\mathrm{gm}} := \boldsymbol{\theta}^{\mathcal{D}} \cup \{\boldsymbol{v}\}$. The GM model then writes:

$$\kappa_{\boldsymbol{\theta}}^{\mathrm{gm}}(\boldsymbol{x}) = \sum_{k \in \mathcal{K}} \sum_{m \in \mathcal{M}_k} v_{km} \, \kappa_{\boldsymbol{\theta}_k}^{\mathrm{sg}}(\boldsymbol{x} - \boldsymbol{x}_{km}) \ . \tag{7}$$

To capture the structure of the dictionary parameter set $\boldsymbol{\theta}^{\mathcal{D}}$, we regroup the kernels in $\mathcal{D}$ and the mixture weights into $n_k^{\mathcal{X}}$-dimensional vectors, denoted $\boldsymbol{\kappa}_k(\boldsymbol{x})$ and $\boldsymbol{v}_k$ respectively. Their m-th elements are the translated kernel $[\boldsymbol{\kappa}_k(\boldsymbol{x})]_m := \kappa_{\boldsymbol{\theta}_k}^{\mathrm{sg}}(\boldsymbol{x} - \boldsymbol{x}_{km})$ and the mixture weight $[\boldsymbol{v}_k]_m := v_{km}$ respectively. Then, the GM model (7) writes:

$$\kappa_{\boldsymbol{\theta}}^{\mathrm{gm}}(\boldsymbol{x}) = \sum_{k \in \mathcal{K}} \boldsymbol{\kappa}_k(\boldsymbol{x})^T \boldsymbol{v}_k \ . \tag{8}$$

We define $\mathrm{supp}(\boldsymbol{v}) := \{(k, m) \in \mathcal{KM} \mid [\boldsymbol{v}]_{km} > 0\}$, the *support of the mixture weights*, and $\mathcal{KM} := \bigcup_{k \in \mathcal{K}} \{k\} \times \mathcal{M}_k$. For a fixed dictionary size, the support of $\boldsymbol{v}$ sets the *effective computational effort* to evaluate the GM model by reducing the number of SG kernel evaluations (*i.e.* the sum in equation (7) runs only over $\mathrm{supp}(\boldsymbol{v})$). The size of the support defines our *measure of efficiency* for the MG model. If the set of kernel positions $\mathcal{X} := \cup_{k \in \mathcal{K}} \mathcal{X}_k$ is aligned with the pixel centres, we call the dictionary *digital*, otherwise we call it *analog*.

b) Virtual source interpretation: We can interpret the GM model within the virtual microscope (VM) framework [34]. The MG model (7) can be rewritten as a superposition of n^{c} convolutions:

$$\kappa_{\boldsymbol{\theta}}^{\mathrm{gm}}(\boldsymbol{x}) \, \mathrm{d}\boldsymbol{x} \, \mathrm{d}t = \sum_{k \in \mathcal{K}} \left(\kappa_{\boldsymbol{\theta}_k}^{\mathrm{sg}} * \sum_{m \in \mathcal{M}_k} v_{km} \delta_{\boldsymbol{x}_{km}} \right) (\mathrm{d}\boldsymbol{x} \times \mathrm{d}t) \ .$$

Using the terminology of [34], the $n_k^{\mathcal{X}}$ light sources modelling the k-th object measure (located at $\boldsymbol{x}_{km}$ and of intensity v_{km}) are *virtual*, in the sense that they do not represent physical light sources, but they approximate a photon flux. This observation leads to a representation of the convolution of the GM model with an arbitrary object that is well-suited for the VM framework [34]: the GM model amounts to approximating the PSF by n^{c} optical systems modelled using κ_k^{sg}. For each system, each point source $(\boldsymbol{x}^{\mathrm{ps}}, \varphi^{\mathrm{ps}})$ is replaced by $n_k^{\mathcal{X}}$ point sources:

$\left\{ (\boldsymbol{x}^{\mathrm{ps}} + \boldsymbol{x}_{k1}, v_{k1} \, \varphi^{\mathrm{ps}}), \ldots, (\boldsymbol{x}^{\mathrm{ps}} + \boldsymbol{x}_{kn_k^{\mathcal{X}}}, v_{kn_k^{\mathcal{X}}} \, \varphi^{\mathrm{ps}}) \right\}$ that are convolved independently with κ_k^{sg}. The resulting mean images are summed to produce the mean image of the original imaging system.

c) Computational efficiency: The GM model can be efficiently evaluated by the FFT or the IFGT (see [39]). The FFT is suitable for the digital scenario when the object model and the PSF model are sampled on the same grid. The IFGT allows fast evaluation of the forward model based on the virtual source formulation discussed above. In both scenarios, the computational efficiency of the evaluation of the Gaussian mixture PSF model depends on the size of its support.

III. INVERSE PROBLEM

We aim to estimate the parameters of the PSF models from calibration data. In scanning fluorescence microscopy, the image stack is acquired by moving the focal plane over the imaging volume [15]. The camera detector of size $n^{\mathrm{h}} \times n^{\mathrm{w}}$ pixels measures the incident light intensity during the exposure time t_e and encodes it into grey values at n^{s} positions of the focal plane. The pixel size and the displacement between two consecutive focal planes are denoted Δ_{xy} and Δ_z, respectively. As a result, the image stack is an array of grey values, denoted $\boldsymbol{Z} \in \mathbb{Z}_+^{n^{\mathrm{s}} \times n^{\mathrm{h}} \times n^{\mathrm{w}}}$, holding measurements from $n^{\mathrm{p}} := n^{\mathrm{s}} n^{\mathrm{h}} n^{\mathrm{w}}$ pixels. We make the standard assumption that the images in a stack are acquired simultaneously in time.

A. Estimation problem: maximum a posteriori formulation

1) Problem formulation: Given a PSF model $\kappa_{\boldsymbol{\theta}}$, we solve a maximum *a posteriori* (MAP) optimisation problem to estimate $\boldsymbol{\theta}$. In general, the position $\boldsymbol{x}^{\mathrm{ps}}$ and intensity φ^{ps} of the PS object are also unknown. Therefore, the general inverse problem aims at jointly estimating the parameters of the PS and the PSF models:

$$\begin{aligned} \underset{\boldsymbol{x}^{\mathrm{ps}}, \, \varphi^{\mathrm{ps}}, \, \boldsymbol{\theta}}{\arg\min} \ & \mathrm{nll}(\boldsymbol{x}^{\mathrm{ps}}, \varphi^{\mathrm{ps}}, \boldsymbol{\theta} \mid \boldsymbol{Z}) + \eta \, \mathrm{R}(\boldsymbol{x}^{\mathrm{ps}}, \varphi^{\mathrm{ps}}, \boldsymbol{\theta}) \\ & \text{s.t.} \ \boldsymbol{x}^{\mathrm{ps}} \in \Omega, \ \varphi^{\mathrm{ps}} \in \mathbb{R}_+, \ \boldsymbol{\theta} \in \Theta \end{aligned} \tag{9}$$

where nll is called the data-fitting term, R the regularisation term encoding our prior knowledge about the model parameters, and η the regularisation parameter controlling the trade-off between them. We call the problem (9) the *parametric blind PS deconvolution*. It specialises to two problems:

a) PS localisation: The PSF is assumed known, and only the position and intensity of the PS are estimated. In this case, the data-fitting term reduces to $\mathrm{nll}(\boldsymbol{x}^{\mathrm{ps}}, \varphi^{\mathrm{ps}} \mid \boldsymbol{Z}, \boldsymbol{\theta})$, and the PSF model parameters are fixed.

b) PSF calibration: The PS is assumed known, and only the PSF model parameters are estimated. The data-fitting term reduces to $\mathrm{nll}(\boldsymbol{\theta} \mid \boldsymbol{Z}, \boldsymbol{x}^{\mathrm{ps}}, \varphi^{\mathrm{ps}})$, and the PS intensity and position are fixed.

2) Data-fitting functional: In a Bayesian setting, the data-fitting term corresponds to the negative log-likelihood (nll) derived from the stochastic image formation model described by (2). We convert the grey values into what we call the *raw photon counts* using (6) and vectorise it into $\boldsymbol{n} :=$

$\mathrm{vec}\big(\nu^{-1}(\boldsymbol{Z})\big) \in \mathbb{R}_+^{n^{\mathrm{p}}}$. Specialising the object-to-pixel mapping defined by (5) for the PSF model parameterised by $\boldsymbol{\theta}$, we compute the *expected photon count* at each pixel $j \in \{1, \ldots, n^{\mathrm{p}}\} =: \mathcal{J}$ and stack the results into a vector, denoted $\boldsymbol{\mu}(\boldsymbol{x}^{\mathrm{ps}}, \varphi^{\mathrm{ps}}, \boldsymbol{\theta}) \in \mathbb{R}_+^{n^{\mathrm{p}}}$. To compare different models, we use the normalised version of the nll, also called *deviance* or *Bregman divergence* [3], which is zero when over-fitting (*i.e.* the model prediction at each pixel is its raw photon count):

$$\mathrm{nll}(\boldsymbol{x}^{\mathrm{ps}}, \varphi^{\mathrm{ps}}, \boldsymbol{\theta} \mid \boldsymbol{Z}) =: \mathrm{nll}(\boldsymbol{x}^{\mathrm{ps}}, \varphi^{\mathrm{ps}}, \boldsymbol{\theta} \mid \boldsymbol{n})$$
$$= \left\langle \boldsymbol{1}_{n^{\mathrm{p}}}, \ \boldsymbol{n} \log \frac{\boldsymbol{n}}{\boldsymbol{\mu}(\boldsymbol{x}^{\mathrm{ps}}, \varphi^{\mathrm{ps}}, \boldsymbol{\theta})} + \boldsymbol{\mu}(\boldsymbol{x}^{\mathrm{ps}}, \varphi^{\mathrm{ps}}, \boldsymbol{\theta}) - \boldsymbol{n} \right\rangle .$$

a) Vector of expected photon counts: The vector of expected photon counts is computed using (5). For the BW and SG models, the formulation is straightforward. However, the GM model requires more attention in its formulation. Substituting (8) into (5), we evaluate the expected photon count at each pixel $j \in \mathcal{J}$ and stack the results into a vector:

$$\boldsymbol{\mu}(\boldsymbol{x}^{\mathrm{ps}}, \varphi^{\mathrm{ps}}, \boldsymbol{\theta}^{\mathrm{gm}}) = \varphi^{\mathrm{ps}} \sum_{k \in \mathcal{K}} \boldsymbol{K}_k(\boldsymbol{x}^{\mathrm{ps}}) \boldsymbol{v}_k + \varphi^{\mathrm{bg}} \boldsymbol{1}_{n^{\mathrm{p}}} , \quad (10)$$

where $\boldsymbol{K}_k$ is the blurring matrix defined for the k-th kernel as:

$$\boldsymbol{K}_k(\boldsymbol{x}^{\mathrm{ps}})^T := [\boldsymbol{\kappa}_k(\boldsymbol{x}_1 - \boldsymbol{x}^{\mathrm{ps}}), \ldots, \boldsymbol{\kappa}_k(\boldsymbol{x}_{n^{\mathrm{p}}} - \boldsymbol{x}^{\mathrm{ps}})] .$$

b) Identifiability of Gaussian mixture weights: From (10) it is apparent that only the product between the PS intensity and the GM weights is identifiable. We define the *net mixture intensity* as $\boldsymbol{\varphi}_k^{\mathrm{net}} := \varphi^{\mathrm{ps}} \boldsymbol{v}_k \in \mathbb{R}_+^{n_k^{\mathcal{X}}}$: the PS intensity is spread among the kernels in the dictionary as virtual intensities. We re-parameterise the vector of expected photon count as $\boldsymbol{\mu}(\boldsymbol{x}^{\mathrm{ps}}, \boldsymbol{\varphi}^{\mathrm{net}}, \boldsymbol{\theta}^{\mathcal{D}}) = \boldsymbol{\mu}(\boldsymbol{x}^{\mathrm{ps}}, \varphi^{\mathrm{ps}}, \boldsymbol{\theta}^{\mathrm{gm}})$, where $\boldsymbol{\varphi}^{\mathrm{net}} \in \mathbb{R}_+^{|\mathcal{D}|}$ is the stacked vector of net mixture intensities.

3) Regularisation functional: In general, the regularisation term R in (9) accounts for the prior knowledge about the PS position and intensity, and the PSF model parameters. However, in this paper we aim at showing how to explore the accuracy–efficiency trade-off based on the GM model. Therefore, we focus on regularising only the PSF model parameters, *i.e.* $\mathrm{R}^{\mathrm{gm}}(\boldsymbol{\theta})$.

One way to trade accuracy for efficiency is to penalise the effective number of Gaussian kernels, by penalising the size of the support of the net mixture intensity vector:

$$\mathrm{R}^{\mathrm{gm}}(\boldsymbol{\varphi}^{\mathrm{net}}) := n^{\mathrm{p}} \sum_{k \in \mathcal{K}} \frac{\eta_k}{\eta} \big| \mathrm{supp}(\boldsymbol{\varphi}_k^{\mathrm{net}}) \big| ,$$

where we scale η by the number of pixels to have a comparable regularisation for different image data. Solving problem (9) with this regularisation functional aims precisely at finding the optimal trade-off between accuracy (minimising the nll) and efficiency (minimising the number of non-zero mixture weights). The regularisation parameters are stacked into a vector, denoted $\boldsymbol{\eta} := (\eta_1, \ldots, \eta_{n^{\mathcal{C}}}) \in \mathbb{R}_+^{n^{\mathcal{C}}}$, and allow exploring this trade-off: small values of $|\boldsymbol{\eta}|$ favour accuracy over efficiency, and large values *vice versa*.

4) Convex relaxation: Problem (9) has multiple sources of non-convexity for the GM model: the joint estimation of PS position and intensity, the PSF parameters estimation, and the cardinality regularisation functional for the GM model. Nevertheless, it has also convex components: the constraint sets are convex, and nll is convex in the mean photon count vector. If the PS position $\boldsymbol{x}^{\mathrm{ps}}$ and the dictionary parameters $\boldsymbol{\theta}^{\mathcal{D}}$ are fixed, the remaining non-convexity is R^{gm}. To handle more tractable problems, we use a convex sparsity-inducing regulariser, denoted $\mathrm{R}_{\mathrm{co}}^{\mathrm{gm}}$, based on the popular ℓ_1 norm [40]:

$$\mathrm{R}_{\mathrm{co}}^{\mathrm{gm}}(\boldsymbol{\varphi}^{\mathrm{net}}) := n^{\mathrm{p}} \sum_{k \in \mathcal{K}} \frac{\eta_k}{\eta} \|\boldsymbol{\varphi}_k^{\mathrm{net}}\|_1 . \quad (11)$$

5) Problem formulation for BW and SG PSF models: For BW and SG, problem (9) amounts to solving the maximum likelihood problem:

$$(\widehat{\boldsymbol{x}}^{\mathrm{ps}}, \widehat{\varphi}^{\mathrm{ps}}, \widehat{\boldsymbol{\theta}}) := \arg\min_{\boldsymbol{x}^{\mathrm{ps}}, \varphi^{\mathrm{ps}}, \boldsymbol{\theta}} \mathrm{nll}(\boldsymbol{x}^{\mathrm{ps}}, \varphi^{\mathrm{ps}}, \boldsymbol{\theta} \mid \boldsymbol{Z})$$
$$\text{s.t. } \boldsymbol{x}^{\mathrm{ps}} \in \Omega, \ \varphi^{\mathrm{ps}} \in \mathbb{R}_+, \ \boldsymbol{\theta} \in \boldsymbol{\Theta} . \quad (12)$$

6) Problem formulation for GM PSF models: We propose solving problem (9) in three steps.

a) PS position estimation, $\widehat{\boldsymbol{x}}^{\mathrm{ps}}$: We solve the *parametric blind PS deconvolution problem* for the SG model given by (12).

b) Mixture weight support estimation: We fix the PS position to its estimated value and solve the *GM PSF calibration problem* using the regulariser (11):

$$\widehat{\boldsymbol{\varphi}}_{\boldsymbol{\eta}}^{\mathrm{net}} := \arg\min_{\boldsymbol{\varphi} \in \mathbb{R}_+^{|\mathcal{D}|}} \mathrm{nll}_{\mathrm{p}}(\boldsymbol{\varphi} \mid \boldsymbol{Z}, \widehat{\boldsymbol{x}}^{\mathrm{ps}}, \boldsymbol{\theta}^{\mathcal{D}}) + \sum_{k \in \mathcal{K}} \eta_k \|\boldsymbol{\varphi}_k\|_1 , \quad (13)$$

where $n^{\mathrm{p}} \mathrm{nll}_{\mathrm{p}} := \mathrm{nll}$. We estimate the support by thresholding the weights above $\varphi_{\min}$:

$$\widehat{\mathrm{supp}}(\widehat{\boldsymbol{\varphi}}_{\boldsymbol{\eta}}^{\mathrm{net}}) := \big\{ (k, m) \in \mathcal{KM} \mid [\widehat{\boldsymbol{\varphi}}_{\boldsymbol{\eta}, k}^{\mathrm{net}}]_m > \varphi_{\min} \big\} .$$

The *effective dictionary* is defined by keeping the kernels in the estimated support:

$$\widehat{\mathcal{D}}_{\boldsymbol{\eta}}^{\mathrm{thr}} := \big\{ \kappa_{\boldsymbol{\theta}_k}^{\mathrm{sg}}(\cdot - \boldsymbol{x}_m) \in \mathcal{D} \mid (k, m) \in \widehat{\mathrm{supp}}(\widehat{\boldsymbol{\varphi}}_{\boldsymbol{\eta}}^{\mathrm{net}}) \big\} . \quad (14)$$

c) Debiasing: The convex problem (13) brings a known problem due to using the ℓ_1 norm: a bias (see *e.g.* [41]) in the intensity estimates $\widehat{\boldsymbol{\varphi}}_{\boldsymbol{\eta}}^{\mathrm{net}}$. We use a refitting strategy based on maximum likelihood to *debias the mixture weights*:

$$\widehat{\boldsymbol{\varphi}}_{\boldsymbol{\eta}}^{\mathrm{deb}} := \arg\min_{\boldsymbol{\varphi} \in \mathbb{R}_+^{|\widehat{\mathcal{D}}_{\boldsymbol{\eta}}^{\mathrm{thr}}|}} \mathrm{nll}\big(\boldsymbol{\varphi} \mid \boldsymbol{Z}, \widehat{\boldsymbol{x}}^{\mathrm{ps}}, \widehat{\mathcal{D}}_{\boldsymbol{\eta}}^{\mathrm{thr}}\big) . \quad (15)$$

We compute the estimates of the PS intensity as $\widehat{\varphi}^{\mathrm{ps}} := \|\widehat{\boldsymbol{\varphi}}_{\boldsymbol{\eta}}^{\mathrm{deb}}\|_1$ and mixture weights as $\widehat{\boldsymbol{v}}_k := (\widehat{\varphi}^{\mathrm{ps}})^{-1} \widehat{\boldsymbol{\varphi}}_{\boldsymbol{\eta}}^{\mathrm{deb}}$.

B. Algorithms

The main difference in solving the parametric blind PS deconvolution problem for different PSF models is the dimensionality of the solution space. For the SG and BW PSF models, problem (12) requires estimating 6 and 7 parameters, respectively. Both are low-dimensional smooth non-convex optimisation problems that can be solved by a general-purpose black-box optimiser. In contrast, the GM PSF calibration

---

Algorithm 1: Fully-split ASB for solving problem (13)

Input : $\boldsymbol{Z}$, φ^{bg}, $\boldsymbol{\eta}$, γ, $\{\boldsymbol{K}_k, \boldsymbol{b}_k^0, \boldsymbol{w}_k^0\}_{k\in\mathcal{K}}$

Output: $\widehat{\boldsymbol{\varphi}}_{\boldsymbol{\eta}}^{\mathrm{net}} := \boldsymbol{w}_3^\infty$

$\forall k \in \mathcal{K}: \boldsymbol{w}_{1k}^0 = \boldsymbol{n},\ \boldsymbol{w}_{2k}^0 = \boldsymbol{w}_{3k}^0 = \boldsymbol{n}_k,\ \boldsymbol{b}_k^0 = \boldsymbol{0}_{n^{\mathrm{p}}+2n_k^{\mathcal{X}}}$

while NOT CONVERGED **do**

  for $k = 1$ **to** $n^{\mathcal{C}}$ **do**

    LS sub-problem:

$$\boldsymbol{\varphi}_k^{i+1} = \arg\min_{\boldsymbol{\varphi}_k} \|\boldsymbol{b}_k^i + \boldsymbol{O}_k\boldsymbol{\varphi}_k - \boldsymbol{w}_k^i\|_2^2 \quad (16)$$

    nll sub-problem:

$$\boldsymbol{w}_{1k}^{i+1} = \mathrm{Prox}_{\gamma\mathrm{nll}_{\mathrm{p}}}\big(\boldsymbol{b}_{1k}^i + \boldsymbol{K}_k(\boldsymbol{x}^{\mathrm{ps}})\boldsymbol{\varphi}_k^{i+1}\big)(17)$$

    ℓ_1–ℓ_2^2 sub-problem:

$$\boldsymbol{w}_{2k}^{i+1} = \mathrm{Prox}_{\gamma\eta_k\|\cdot\|_1}(\boldsymbol{b}_{2k}^i + \boldsymbol{\varphi}_k^{i+1}) \quad (18)$$

    Positivity constraint sub-problem:

$$\boldsymbol{w}_{3k}^{i+1} = \mathrm{Proj}_{\mathbb{R}_+^{n_k^{\mathcal{X}}}}(\boldsymbol{b}_{3k}^i + \boldsymbol{\varphi}_k^{i+1}) \quad (19)$$

    Bregman update (dual gradient ascent):

$$\boldsymbol{b}_k^{i+1} = \boldsymbol{b}_k^i + \boldsymbol{O}_k\boldsymbol{\varphi}_k^{i+1} - \boldsymbol{w}_k^{i+1} \quad (20)$$

  end

end

---

problem (13) is a large-scale non-differentiable convex optimisation problem. We derive an efficient and modular algorithm to solve (13) based on the alternating split Bregman strategy, and discuss the algorithms for the debiasing step.

1) Estimating the support of MG PSF model: We define the energy functional in problem (13) as:

$$\mathcal{E}(\boldsymbol{\varphi}) := \mathrm{nll}_{\mathrm{p}}(\boldsymbol{\varphi} \mid \boldsymbol{Z}, \widehat{\boldsymbol{x}}^{\mathrm{ps}}, \boldsymbol{\theta}^{\mathcal{D}}) + \sum_{k\in\mathcal{K}} \eta_k\|\boldsymbol{\varphi}_k\|_1 + \iota_{\mathcal{S}}(\boldsymbol{\varphi}) ,$$

where $\iota_{\mathcal{S}}(\boldsymbol{\varphi})$ with $\mathcal{S} := \mathbb{R}_+^{|\mathcal{D}|}$ is the indicator functional that assumes 0 if $\boldsymbol{\varphi}$ is componentwise non-negative and $+\infty$ otherwise. This problem has an additive structure at two levels. First, the functional is the sum of three terms: the nll, the ℓ_1 regulariser, and the indicator function $\iota_{\mathcal{S}}(\boldsymbol{\varphi})$. The second level of additivity comes from the sum over kernels in the mean vector (10). We exploit this additivity structure and derive the algorithm in three steps:

a) Operator splitting: We exploit the first level of additivity by introducing dummy variables to split the different terms: $\boldsymbol{w}_k = \begin{bmatrix}\boldsymbol{w}_{1k}^T & \boldsymbol{w}_{2k}^T & \boldsymbol{w}_{3k}^T\end{bmatrix}^T := \boldsymbol{O}_k\boldsymbol{\varphi}_k^{\mathrm{net}} \in \mathbb{R}^{n^{\mathrm{p}}+2n_k^{\mathcal{X}}}$ with $\boldsymbol{O}_k := \begin{bmatrix}\boldsymbol{K}_k^T(\widehat{\boldsymbol{x}}^{\mathrm{ps}}) & \boldsymbol{I}_{n_k^{\mathcal{X}}} & \boldsymbol{I}_{n_k^{\mathcal{X}}}\end{bmatrix}^T \in \mathbb{R}^{(n^{\mathrm{p}}+2n_k^{\mathcal{X}})\times n_k^{\mathcal{X}}}$, where $\boldsymbol{I}_{n_k^{\mathcal{X}}} \in \mathbb{R}^{n_k^{\mathcal{X}}\times n_k^{\mathcal{X}}}$ is the identity matrix. We define the stacked vector $\boldsymbol{w} \in \mathbb{R}^{n^{\mathcal{C}}n^{\mathrm{p}}+2|\mathcal{D}|}$ and the block-diagonal matrix $\boldsymbol{O} := \mathrm{diag}(\boldsymbol{O}_1,\dots,\boldsymbol{O}_{n^{\mathcal{C}}}) \in \mathbb{R}^{(n^{\mathcal{C}}n^{\mathrm{p}}+2|\mathcal{D}|)\times|\mathcal{D}|}$, such that $\boldsymbol{w} = \boldsymbol{O}\boldsymbol{\varphi}^{\mathrm{net}}$. In addition, we denote the subset of dummy variables for the operator $o \in \{1, 2, 3\}$ stacked into a vector as $\boldsymbol{w}_{o:} := \mathrm{vec}(\{\boldsymbol{w}_{ok}\}_{k\in\mathcal{K}})$. We can rewrite energy $\mathcal{E}(\boldsymbol{\varphi})$ to highlight its additive structure: $\mathcal{E}(\boldsymbol{w}) := \mathcal{E}(\boldsymbol{w}_{1:}, \boldsymbol{w}_{2:}, \boldsymbol{w}_{3:}) := \mathrm{nll}_{\mathrm{p}}(\boldsymbol{w}_{1:}) + \sum_{k\in\mathcal{K}} \eta_k\|\boldsymbol{w}_{2k}\|_1 + \iota_{\mathcal{S}}(\boldsymbol{w}_{3k})$, where for simplifying

the notations, we implicitly assume the conditional dependence of $\mathrm{nll}_{\mathrm{p}}$ on the image data $\boldsymbol{Z}$, the estimated point source position $\widehat{\boldsymbol{x}}^{\mathrm{ps}}$, and the dictionary parameters $\boldsymbol{\theta}^{\mathcal{D}}$.

b) Fully-split Bregman: The next step is to fully split $\boldsymbol{w}$ from $\boldsymbol{\varphi}^{\mathrm{net}}$ by applying split Bregman to the equivalent problem $\arg\min_{\boldsymbol{\varphi},\boldsymbol{w}} \langle\boldsymbol{0}_{|\mathcal{D}|}, \boldsymbol{\varphi}\rangle + \mathcal{E}(\boldsymbol{w})$, writing at iteration $i+1$:

$$(\boldsymbol{\varphi}^{i+1}, \boldsymbol{w}^{i+1}) = \arg\min_{\boldsymbol{\varphi},\boldsymbol{w}} \langle\boldsymbol{0}_{|\mathcal{D}|}, \boldsymbol{\varphi}\rangle + \Psi^i(\boldsymbol{\varphi}, \boldsymbol{w})$$
$$\boldsymbol{b}^{i+1} = \boldsymbol{b}^i + \boldsymbol{O}\boldsymbol{\varphi}^{i+1} - \boldsymbol{w}^{i+1} ,$$

where $\Psi^i(\boldsymbol{\varphi}, \boldsymbol{w}) := \mathcal{E}(\boldsymbol{w}) + (2\gamma)^{-1}\|\boldsymbol{b}^i + \boldsymbol{O}\boldsymbol{\varphi} - \boldsymbol{w}\|_2^2$, $\boldsymbol{b} \in \mathbb{R}^{n^{\mathcal{C}}n^{\mathrm{p}}+2|\mathcal{D}|}$ is the vector of the Bregman dual variables stacked similarly to $\boldsymbol{w}$, and γ is the dual-ascent step-size.

c) Gauss-Seidel-like alternation: We exploit the second level of additivity by splitting over the kernels the optimisation problem in the Bregman iteration. The algorithm at iteration i for kernel k reads:

$$\boldsymbol{\varphi}_k^{i+1} = \arg\min_{\boldsymbol{\varphi}_k} \langle\boldsymbol{0}_{|\mathcal{D}|}, \boldsymbol{\varphi}_k\rangle + \frac{1}{2\gamma}\|\boldsymbol{b}_k^i + \boldsymbol{O}_k\boldsymbol{\varphi}_k - \boldsymbol{w}_k^i\|_2^2 \quad (21)$$

$$\boldsymbol{w}_k^{i+1} = \arg\min_{\boldsymbol{w}_k} \mathcal{E}_k^i(\boldsymbol{w}_k) + \frac{1}{2\gamma}\|\boldsymbol{b}_k^i + \boldsymbol{O}_k\boldsymbol{\varphi}_k^{i+1} - \boldsymbol{w}_k\|_2^2$$
$$=: \mathrm{Prox}_{\gamma\mathcal{E}_k^i}(\boldsymbol{b}_k^i + \boldsymbol{O}_k\boldsymbol{\varphi}_k^{i+1}) \quad (22)$$
$$\boldsymbol{b}_k^{i+1} = \boldsymbol{b}_k^i + \boldsymbol{O}_k\boldsymbol{\varphi}_k^{i+1} - \boldsymbol{w}_k^{i+1} . \quad (23)$$

where the energy $\mathcal{E}_k^i(\boldsymbol{w}_k)$ introduces the coupling between kernels and relies on the set of $k - 1$ weights that are already updated at the i-th iteration: $\mathcal{E}_k^i(\boldsymbol{w}_k) := \mathrm{nll}_{\mathrm{p}}(\dots, \boldsymbol{w}_{1k-1}^{i+1}, \boldsymbol{w}_{1k}, \boldsymbol{w}_{1k+1}^i, \dots) + \eta_k\|\boldsymbol{w}_{2k}\|_1 + \iota_{\mathcal{S}}(\boldsymbol{w}_{3k})$.

d) Sub-problems solution: The fully-split ASB strategy amounts to solving three standard problems: a least-squares (LS) problem (21), a proximal map evaluation (22), and a linear update (23). Further, it leads to a decomposition of the proximal map (22) in three independent proximal maps (17), (18), and (19), that decouple across pixels. The algorithm is shown in Algorithm 1, where $\boldsymbol{n}_k$ denotes the image data at the virtual source positions.

The solution to the LS sub-problem (21) is straightforward:

$$\boldsymbol{w}_k^{i+1} = (\boldsymbol{O}_k^T\boldsymbol{O}_k)^{-1}\boldsymbol{O}_k^T(\boldsymbol{w}_k^i - \boldsymbol{b}_k^i) , \quad (24)$$

with $\boldsymbol{O}_k^T\boldsymbol{O}_k = 2\boldsymbol{I}_{n^{\mathcal{X}}} + \boldsymbol{K}_k^T\boldsymbol{K}_k$ and $\boldsymbol{O}_k^T(\boldsymbol{w}_k^i - \boldsymbol{b}_k^i) = \boldsymbol{K}_k^T(\boldsymbol{w}_{1k}^i - \boldsymbol{b}_k^i) + \boldsymbol{w}_{2k}^i - \boldsymbol{b}_{2k}^i + \boldsymbol{w}_{3k}^i - \boldsymbol{b}_{3k}^i$, where $\boldsymbol{K}_k := \boldsymbol{K}_k(\boldsymbol{x}^{\mathrm{ps}})$. The inverse operator can be pre-computed outside the main iteration. Moreover, digital dictionaries can be efficiently evaluated using a spectral solver based on the FFT.

The proximal maps (18) and (19) are also known: (18) is a componentwise soft-thresholding of $\boldsymbol{b}_{2k}^i + \boldsymbol{\varphi}_k^{i+1}$ with threshold $\gamma\eta_k$, and (19) is a componentwise projection of $\boldsymbol{b}_{3k}^i + \boldsymbol{\varphi}_k^{i+1}$ on $\mathbb{R}_+$. The solution to the proximal (17) is derived in [42], [3]. However, due to the additive structure of the mean vector and the Gauss-Seidel-like alternation, we provide more details for this proximal.

At iteration i, when the alternation reaches kernel k, the mean vector (10) can be rewritten in terms of the dummy variables:

$$\boldsymbol{\mu}_k^{i+1} := \sum_{k'=1}^{k-1} \boldsymbol{w}_{1k'}^{i+1} + \boldsymbol{w}_{1k} + \sum_{k'=k+1}^{n^{\mathcal{C}}} \boldsymbol{w}_{1k'}^i + \varphi^{\mathrm{bg}} \mathbf{1}_{n^{\mathrm{p}}} =: \boldsymbol{w}_{1k} + \boldsymbol{r}_k^{i+1} \ .$$

Instead of solving (17) in terms of $\boldsymbol{w}_{1k}$, we solve the problem in terms of $\boldsymbol{\mu}_k$ and update $\boldsymbol{w}_{1k}^{i+1}$ by subtracting the residuals $\boldsymbol{r}_k^{i+1}$:

$$\boldsymbol{\mu}_k^{i+1} = \mathrm{Prox}_{\gamma \mathrm{nll}_{\mathrm{p}}}\left(\boldsymbol{b}_{1k}^i + \boldsymbol{K}_k \boldsymbol{\varphi}_k^{i+1} + \boldsymbol{r}_k^{i+1} \right) \quad (25)$$

$$\boldsymbol{w}_{1k}^{i+1} = \boldsymbol{\mu}_k^{i+1} - \boldsymbol{r}_k^{i+1} \ . \quad (26)$$

Evaluating (25) amounts to choosing the positive solution of the following quadratic equation in $[\boldsymbol{\mu}_k]_j$ defined for the j-th pixel:

$$[\boldsymbol{\mu}_k]_j^2 + \left(\frac{\gamma}{n^{\mathrm{p}}} - \boldsymbol{e}_j^T \boldsymbol{c}_k^i \right) - \frac{\gamma}{n^{\mathrm{p}}} [\boldsymbol{n}_k]_j = 0 \ ,$$

with $\boldsymbol{c}_k^i := \boldsymbol{b}_k^i + \boldsymbol{K}_k \boldsymbol{\varphi}_k^{i+1} + \boldsymbol{r}_k^{i+1}$.

2) Debiasing mixture weights of MG PSF model: The gradient of nll with respect to the mixture weights can be derived analytically:

$$\partial_{\boldsymbol{\varphi}_k} \mathrm{nll}(\boldsymbol{\varphi}) = \sum_{j=1}^{n^{\mathrm{p}}} \left(1 - \frac{[\boldsymbol{n}_k]_j}{[\boldsymbol{\mu}(\boldsymbol{x}^{\mathrm{ps}}, \boldsymbol{\varphi})]_j} \right) \boldsymbol{K}_k^T \boldsymbol{e}_j \ .$$

To solve (15), we use gradient-based algorithms allowing positivity constrains.

IV. EXPERIMENTS

A. Illustrative example: synthetic 1-D

1) Imaging settings: We place an idealised PS object at $\boldsymbol{x}^{\mathrm{ps}} = (2.5\,\mu\mathrm{m}, 0\,\mu\mathrm{m}, 1.5\,\mu\mathrm{m})$ in the 3D imaging volume. We model the optical distortions using the BW PSF. Using the forward problem in Section II, we model the signal acquired by a one-dimensional camera detector along the x-axis in the range $x \in [0\,\mu\mathrm{m}, 5\,\mu\mathrm{m}]$, at $y = z = 0\,\mu\mathrm{m}$ (the imaging parameters are summarised in Table I). This one-dimensional synthetic signal captures realistic features found in experimental PSF image data: a prominent central mode with side lobes that are characterised by a rich structure and an amplitude significantly above the background signal. In what follows, we assume the background intensity known.

2) SG model: We solve the parametric blind PS deconvolution problem using the covariance matrix adaptation evolutionary strategy (CMA-ES) algorithm [43]. It is a popular and well-tested derivative-free algorithm designed to solve low-to-moderate dimensional non-convex optimisation problems (Fig. 2a). We observe that the estimated PS position $(\hat{x} = 2.539\,\mu\mathrm{m})$ is close to the true value. However, the approximation accuracy of the central mode is poor: its width is overestimated resulting in an underestimated intensity.

3) GM model with a one-kernel dictionary: We use a digital dictionary, denoted $\mathcal{D}_1^{\mathrm{1d}}$, made of Gaussian kernels of standard deviation $0.1\,\mu\mathrm{m}$, placed at every pixel centres, *i.e.* $\boldsymbol{\theta}^{\mathcal{D}_1^{\mathrm{1d}}} = \{0.1\} \times \{\boldsymbol{x}_j\}_{j \in \mathcal{J}}$. We estimate the net mixture intensities by applying Algorithm 1 for different values of the regularisation parameter and build the GM model by using a threshold of $\varphi_{\min} = 0.1$ in (14). The results are shown on Fig. 2b. For smaller regularisation, the estimated support of the GM model covers the support of the true signal. For higher regularisation, the estimated support overlaps only with the regions of high signal: the central mode and side lobes for $\eta_1 = 0.04$, only the central mode for $\eta_1 = 0.07$. However, we observe that the estimated intensity is biased, as expected (see Section III-A6c).

We solve problem (15) using CMA-ES and two gradient-based algorithms that allow enforcing positivity constraints: Levenberg-Marquardt (LM), and the limited-memory Broyden–Fletcher–Goldfarb–Shanno algorithm with box constraints (L-BFGS-B). The three algorithms result in similar reconstructions, but L-BFGS-B has the lowest run-time (Fig. 2). We observe that the debiasing step induces even more sparsity.

The estimated GM model improves compared to SG model in two ways: the width and intensity of the central lobe are accurately reconstructed, even for a high regularisation, *i.e.* when the PSF is modelled with only a few kernels; for smaller regularisation, the GM model also captures the side lobes.

4) GM model with a two-kernel dictionary: We add to the previous dictionary a second kernel of standard deviation $0.2\,\mu\mathrm{m}$ such that the new dictionary, denoted $\mathcal{D}_2^{\mathrm{1d}}$, has parameters $\boldsymbol{\theta}^{\mathcal{D}_2^{\mathrm{1d}}} = \boldsymbol{\theta}^{\mathcal{D}_1^{\mathrm{1d}}} \cup \{0.2\} \times \{\boldsymbol{x}_j\}_{j \in \mathcal{J}}$. Similarly to the one-kernel dictionary, we observe that the amount of regularisation controls the number of each kernel in the effective dictionary (Fig. 3a). If the regularisation is equally increased for both kernels (plots on the diagonal), the support size decreases. For a higher regularisation ($\eta_1 = \eta_2 = 0.07$), only the smaller kernel contributes to modelling the PSF. If the regularisation parameter of one kernel changes, the cardinality of the support of the other kernel remains the same. At the debiasing step, if the regularisation parameter for both kernels are equal, the preference is given to the smaller kernel as it allows capturing finer details of the PSF (Fig. 3b, plots on the diagonal). When we regularise more the smaller kernel, the bigger kernel is used to approximate the wider lobes, whereas the smaller kernel is used to approximate the narrow central mode (Fig. 3b, $\eta_1 = 0.04$, $\eta_2 = 0.01$).

B. GM PSF model: exploring accuracy–efficiency trade-off

The one-dimensional synthetic example illustrates how the GM model improves the model accuracy compared to SG, while controlling the model complexity by designing the dictionary structure (*i.e.* one/two kernels) and the amount of regularisation. We now apply our framework to three-dimensional image data: a synthetic image stack generated by a BW model, and real fluorescent bead measurements acquired by a widefield and a laser scanning confocal microscope.

1) Imaging settings: The parameter of the image formation process are summarised in Table I.

Table I
PARAMETERS OF THE IMAGE FORMATION PROCESS

Dataset	Object-to-pixel			Sampling				Pixel-to-image				Object
	λ [nm]	NA	n_i	$n^h \times n^w \times n^s$	Δ_{xy} [nm]	Δ_z [nm]	t_e [ms]	q_λ	M	f	b	diameter [nm]
Synthetic 1-D	474	1.45	1.518	$1 \times 101 \times 1$	50	–	1	1	1	1	0	δ
SBW	474	1.45	1.518	$81 \times 81 \times 101$	65	200	21	0.81	1	2.0	100	δ
WFFM	620	1.45	n.a.	$81 \times 81 \times 31$	65	200	21	0.81	1	2.14	98.24	50
LSCM	520	1.45	n.a.	$61 \times 61 \times 101$	133	50	12	0.70	200	6.44	398.06	100

(a) SG PSF.   (b) GM PSF before debiasing.   (c) Run-time of the debiasing step.

(d) GM PSF debiased using CMA-ES.   (e) GM PSF debiased using LM.   (f) GM PSF debiased using L-BFGS-B.
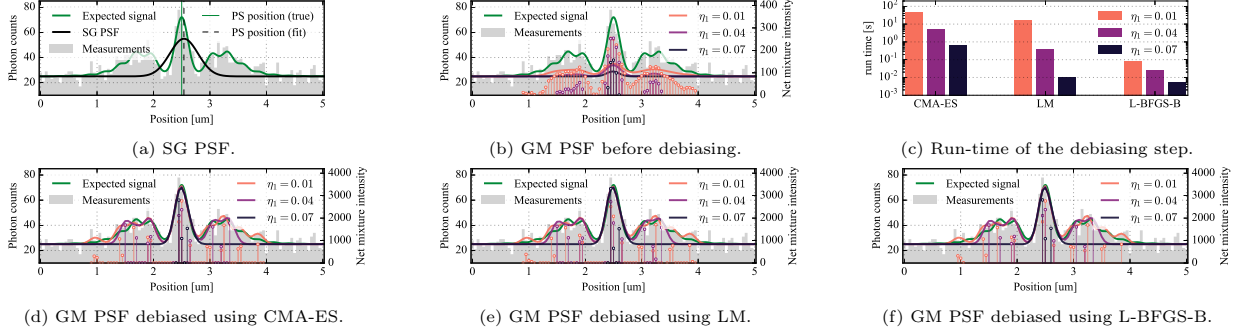
Figure 2. **SG PSF model and GM PSF model with a one-kernel dictionary for a one-dimensional synthetic signal.** (a) Parametric blind PS deconvolution for the SG model. (b) GM model (continuous line) and mixture weights support (weighted Dirac comb shown as vertical bars) estimated using Algorithm 1 for different amount of regularisation. (c) Run-time of debiasing using the covariance matrix evolution evolution strategy (CMA-ES), the Levenberg-Marquardt (LM) and the limited-memory Broyden–Fletcher–Goldfarb–Shanno algorithm with box constraints (L-BFGS-B). (d) - (f) GM model after debiasing.

(a) Before debiasing.
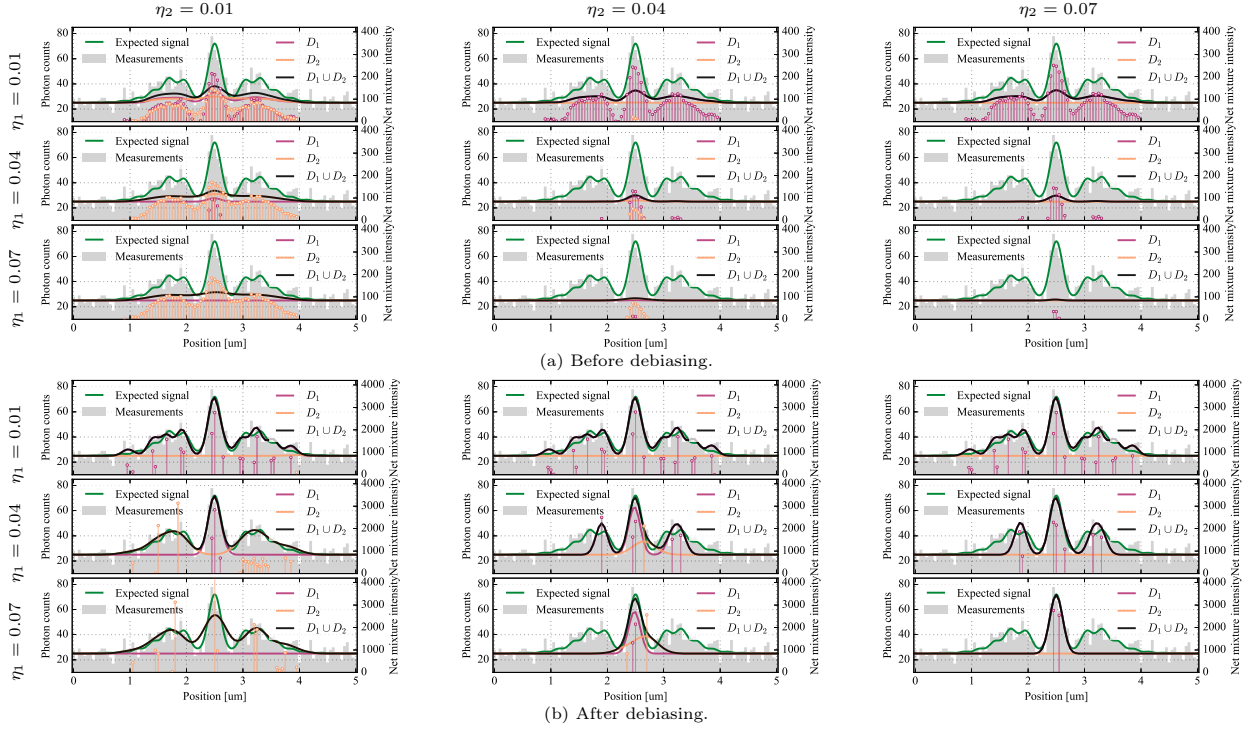
(b) After debiasing.

Figure 3. **GM PSF model with a two-kernel dictionary for a one-dimensional synthetic signal.** The GM model (continuous line) and the underlying mixture weights (weighted Dirac comb shown as vertical bars) are estimated using Algorithm 1 for different amount of regularisation before (a) and after (b) debiasing. The GM models are evaluated separately for the smaller kernel (purple), the bigger kernel (orange), and both kernels (black).

a) Synthetic Born and Wolf (SBW): We use the VM framework [34] and the forward problem in Section II-A to simulate an image stack of an idealised PS object. We simulate an idealised microscope governed by a BW PSF model, resulting in the image stack shown in Fig. 1a.

b) Widefied fluorescence microscopy (WFFM): SPHERO^{TM} fluorescent beads of $50\,nm$ in diameter (excitation wavelength: $576\,nm$) were imaged using a widefield setup equipped with a CMOS camera ORCA-Flash 4.0 V2 (Hamamatsu). We manually selected a region

Table II
ESTIMATED AND THEORETICAL SG PSF MODELS COMPARISON

Dataset	Estimated parameters		Theoretical parameters	
	(σ_{xy}, σ_z) [nm]	nll	(σ_{xy}, σ_z) [nm]	nll
SBW	$(262, 842)$	3.82e+5	$(74, 267)$	5.44e+5
WFFM	$(400, 801)$	3.78e+5	$(96, 349)$	5.34e+5
LSCM	$(247, 512)$	5.50e+5	$(63, 229)$	17.2e+5

Table III
DESIGNS OF DICTIONARIES WITH A SINGLE KERNEL

Dataset	Parameters (σ_{xy}, σ_z) [nm]			
	$\mathcal{D}_1$	$\mathcal{D}_2$	$\mathcal{D}_3$	$\mathcal{D}_4$
SBW	$(262, 842)$	$(131, 421)$	$(87, 281)$	$(66, 210)$
WFFM	$(400, 801)$	$(200, 401)$	$(133, 267)$	$(100, 200)$
LSCM	$(246, 509)$	$(123, 255)$	–	–

containing one bead, resulting in the image stack in Fig. 1b.

c) Laser scanning confocal microscopy (LSCM): Tetraspeck™ fluorescent beads of $100\,\mathrm{nm}$ in diameter (excitation wavelength: $488\,\mathrm{nm}$) were acquired using a confocal setup equipped with an alpha Plan-Apochromat 100x/1.46 Oil DIC M27 objective (Carl Zeiss) and an Evolve 512 Delta EM-CCD camera (Photometrics). We manually selected a region containing one bead, resulting in the image stack in Fig. 1c.

2) Estimating the background intensity: We estimate the background intensity by computing the median of the raw photon count n_k and divide it by the integration volume c.

3) SG model: We solve the parametric blind PS deconvolution problem using CMA-ES (SG). We compare the estimated standard deviations with the theoretical values of the SG model derived in [26] (SGT): the parameters are overestimated due to the rich structure of the side lobes (similar to the effect observed in the 1D synthetic example in Fig. 2a) but results in a lower nll (Table II). The two models are show on Fig. 6.

4) GM model with a one-kernel dictionary: We design four digital dictionaries for SBW and WFFM and two dictionaries for LSCM based on the Gaussian kernel estimated by fitting a SG model parameterised by $\widehat{\boldsymbol{\theta}}^{\mathrm{sg}}$. The dictionaries are defined from this estimate by reducing the kernel size, and placing each kernel at every pixel centre. The parameters for dictionary d are $\boldsymbol{\theta}^{\mathcal{D}_d} := \{\widehat{\boldsymbol{\theta}}^{\mathrm{sg}}/d\} \times \{\boldsymbol{x}_j\}_{j \in \mathcal{J}}$. The digital dictionaries allow computing the solution of the LS sub-problem (24) efficiently with a spectral solver based on the FFT. We use reflexive boundary conditions and diagonalise the operators $\boldsymbol{O}_k$, $\boldsymbol{O}_k^T$, and $\boldsymbol{O}_k^T\boldsymbol{O}_k$ (thanks to central symmetry of the Gaussian kernels) using the discrete cosine transform II [44], [45]. The dictionary parameters are summarised in Table III.

We vary the amount of regularisation to explore the trade-off between accuracy and efficiency of the GM model (Fig. 4). We apply Algorithm 1 to estimate the net mixture intensity, obtain the effective dictionary by thresholding the weights above $\varphi_{\min} := y_{\min} c^{-1}\sqrt{8\pi^3\sigma_{xy}^4\sigma_z^2}$, where $y_{\min}$ is the 99th percentile of the Poisson distribution with mean intensity $c\varphi_t^{\mathrm{bg}}$, and debias the mixture weight using L-BFGS-B. Examples of the estimated PSF models are shown in Fig. 6. We observe that for $\mathcal{D}_1$, *i.e.* when the dictionary is built from the

kernel estimated by fitting the SG model to localise the bead, the effective dictionary is small, and its size barely depends on the regularisation and is comparable with the SG model in accuracy. If the dictionary is built from smaller kernels, the regularisation parameter controls the number of Gaussian kernels: for low regularisation the support of the mixture weights is large and the model overfits (*e.g.* GM1 for SBW), whereas increasing the regularisation reduces overfitting while capturing the PSF lobes (*e.g.* GM2 for SBW). From the highest density region (HDR) plots [46], we observe that the kernels are placed at high-signal regions. When the regularisation increases, kernels are removed from the lower-signal regions.

These observations are consistent with the literature: in [26], it has been shown that no accurate Gaussian approximation exists for a 3D WFFM PSF, whereas an SG approximation is nearly perfect for LSCM. Comparing the accuracy of the GM and SG models, we observe that the former brings significant improvement for WFFM and only a slight improvement for LSCM (Fig. 4).

5) GM model with a two-kernel dictionary: We built the two-kernel dictionaries by merging single-kernel dictionaries: $\mathcal{D}_2 \cup \mathcal{D}_3$ for SBW and WFFM, $\mathcal{D}_1 \cup \mathcal{D}_2$ for CLSM. We explore the accuracy–efficiency trade-off by varying the regularisation parameter of each kernel in the dictionary (Fig. 5). We notice that similarly to the one-dimensional case, the preference is given to smaller kernels: they mostly determine the efficiency and the accuracy of the GM model. However, adding a larger kernel decreases the effective dictionary size, hence increasing the efficiency. We investigate the spatial distribution of each kernel in the dictionary by computing the empirical probability map that a kernel is selected at a given pixel among the reconstructions across all regularisation parameter combinations. We observe that the larger kernels are selected at a few positions only, near the centre of the PSF, whereas smaller kernels are mostly positioned at the side lobes.

6) GM model: robustness to the measurement noise: We simulate 50 independent realisations of the noise model to generate synthetic image of an idealised PS object using the BW PSF model as described in Section IV-B1a. We estimate the GM PSF models using the same dictionary and regularisation parameters as for the GM1, GM2, and GM3 models displayed in Fig. 4a and Fig. 5a. As expected, the size of the support and the associated kernel locations in the estimated PSF models vary across the noise realisations. To assess the robustness of the GM PSF reconstruction, we investigate the variability in the estimated mixtures indirectly, by projecting the PSF model on the pixel grid using (10), where we set the background intensity to zero. We compute the mean and standard deviation over the estimated image stacks (Fig. 7a and Fig. 7b). We observe that the model consistently captures the overall PSF shape including the tails (Fig. 7a). However, variations remains in the estimated PSF models, mainly in the tails where the signal is dimmer: in these regions noise has a larger effect on the position and weight of the estimated Gaussian kernels (Fig. 7b).

In addition, to assess the robustness in the mixture weights, we compute for each independent realisation the histogram of the estimated mixture weights (Fig. 7c). For each bin we

(a) Synthetic Born and Wolf

(b) Widefied fluorescence microscopy
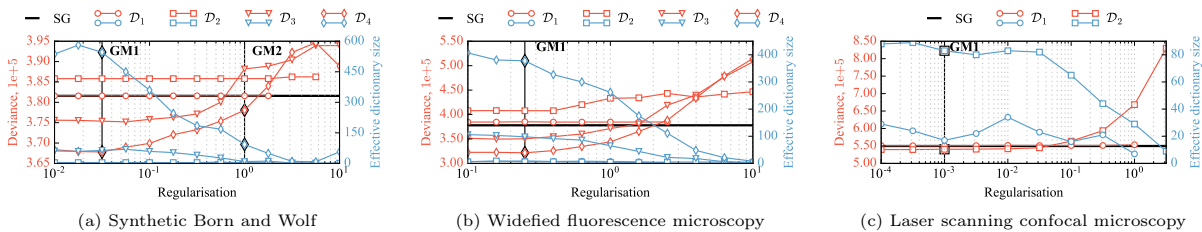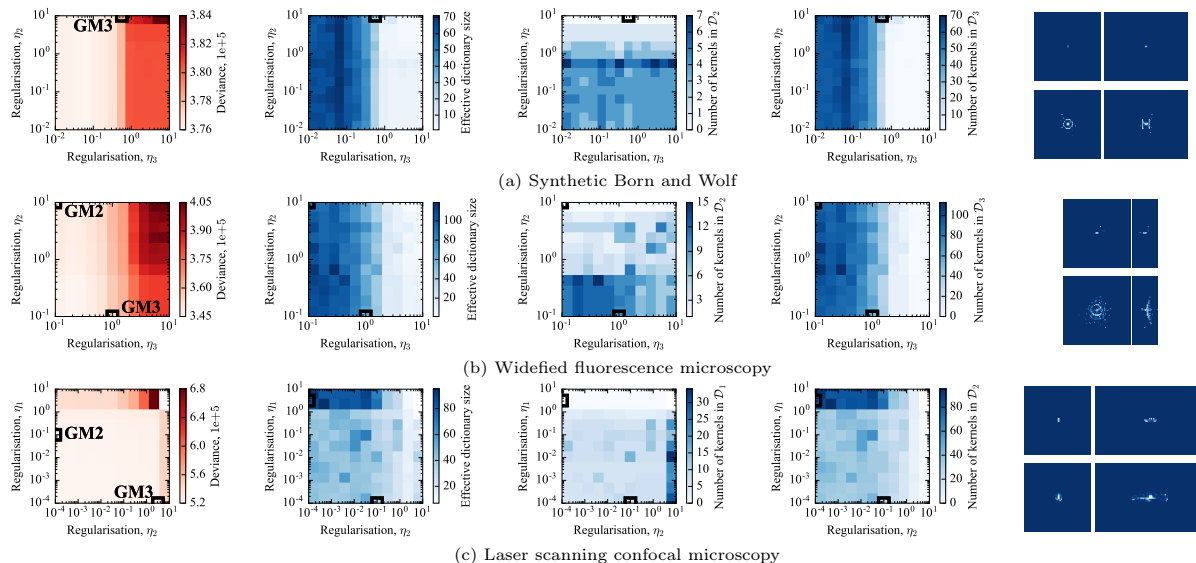
(c) Laser scanning confocal microscopy

Figure 4. **Trade-off between accuracy and efficiency for the GM model with one-kernel dictionaries.** Results shown for the three datasets in Fig. 1 and the digital dictionaries for different kernel size (SBW and WFFM: $\mathcal{D}_1$, $\mathcal{D}_2$, $\mathcal{D}_3$, $\mathcal{D}_4$; LSCM: $\mathcal{D}_1$, $\mathcal{D}_2$, see Table III). For each dictionary, we explore the trade-off between *accuracy* (measured as the deviance) and *efficiency* (measured as the effective dictionary size) by varying the *regularisation parameter*: the higher the regularisation, the lower the size, the higher the efficiency, the lower the accuracy. The horizontal black line indicates the deviance of the SG model estimated by solving the parametric blind PS deconvolution problem (see Section IV-B3). We show examples of models referenced as **GM(.)** on Fig. 6.

(a) Synthetic Born and Wolf

(b) Widefied fluorescence microscopy

(c) Laser scanning confocal microscopy

Figure 5. **Trade-off between accuracy and efficiency for the GM model with two-kernel dictionaries.** Results shown for the three datasets in Fig. 1 and the digital dictionaries constructed from the one-kernel dictionaries used in Fig. 4 (SBW and WFFM: $\mathcal{D}_2 \cup \mathcal{D}_3$; CLSM: $\mathcal{D}_1 \cup \mathcal{D}_2$). We vary the amount of regularisation of each kernel in the dictionary to explore the trade-off between the *accuracy* (column 1) and the *efficiency* (column 2). For each amount of regularisation, we also show the number of larger (column 3) and smaller (column 4) kernels in the effective dictionary. We compute the probability at each pixel of selecting a larger (column 5, top) or a smaller (column 5, bottom) kernel across all regularisation parameters. The plots display orthogonal z- and x-maximum projections of the probabilities. We show examples of models referenced as **GM(.)** on Fig. 6.

(a) Synthetic Born and Wolf

(b) Widefied fluorescence microscopy
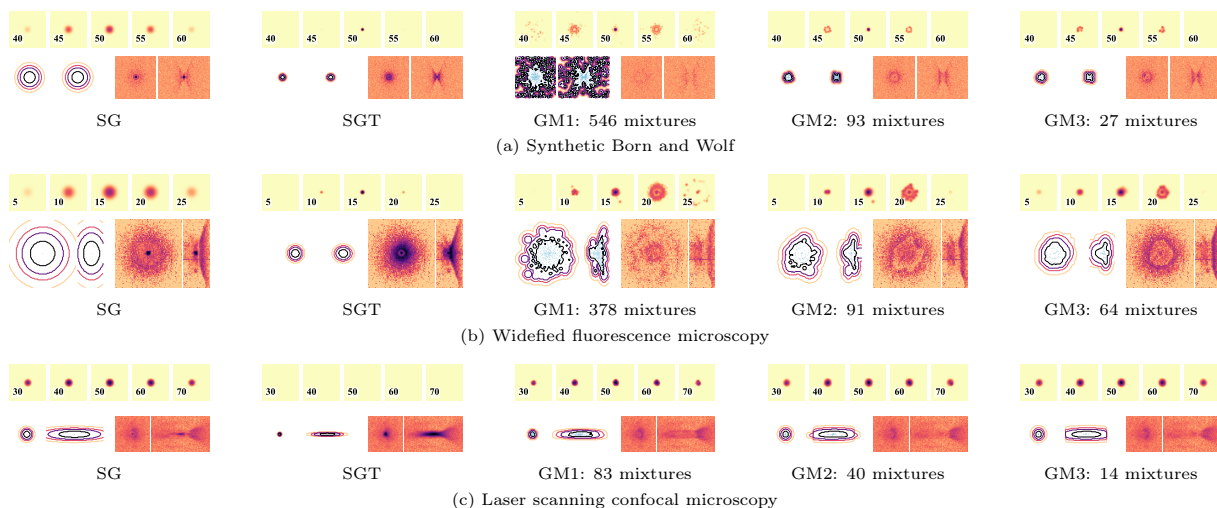
(c) Laser scanning confocal microscopy

Figure 6. **Examples of SG, SGT and GM PSF models.** PSF models reconstructed from the datasets shown in Fig. 1: empirical SG model parametrised by solving the blind PS deconvolution (SG), theoretical SG model (SGT) and three GM models (GM1, GM2, GM3) selected as shown in Fig. 4 and Fig. 5. For each PSF model, the panel is organised as follows. *First row:* selected image slices corresponding to the same focal planes as in Fig. 1. *Second row left:* highest density region (HDR) plot projected orthogonally along z- and x-axis. The HDR plots display the following quantiles for the isolines: 0.0, 0.5, 0.75, 0.95. *Second row right:* orthogonal z- and x- projections of the deviance computed between the expected and the raw photon counts.

(a) Mean image

(b) STD image

(c) Statistics of mixture weights

Figure 7. **Robustness of the GM PSF model reconstruction to the measurement noise.** We estimate the GM PSF models from image stacks of a point source generated using the BW PSF model for 50 independent realisations of the noise model. We use the same dictionaries and regularisation parameters as for GM1, GM2, and GM3 models in Fig. 4a and Fig. 5a. We sample the estimated PSF models and display orthogonal z- and x- mean projections of mean (a) and standard deviation (a) over the image stacks. In (c), we show the variability of the mixture weights histogram by showing the Fano factor (variance over mean of the count in each bin).

TABLE IV
ACCURACY–EFFICIENCY TRADE-OFF

Model	Accuracy	Efficiency	Run-time [s][a]	
	nll	$|\mathrm{supp}(\boldsymbol{\varphi})|$	mean	std
BW[b]	3.55e+5	–	442.5772	5.226578
SG	3.82e+5	–	0.031730	0.000878
SGT	3.94e+5	–	0.032802	0.000217
GM1	3.68e+5	546	0.155430	0.001401
GM2	3.78e+5	93	0.050053	0.001265
GM3	3.80e+5	27	0.041315	0.000756

[a] Statistics computed on 100 images of size $81 \times 81 \times 101$ pixels. Ran on an Intel(R) i7-4770 CPU (3 GHz) with 8 cores.
[b] Unoptimised python implementation. For comparison, the approximation implemented in [47] yields a typical run-time of 2.3 s on Intel Core i7 (2.5 GHz) with 4 cores.

compute the mean and variance of the number of kernels falling into it and compute the Fano factor (variance over mean of the count) to capture the variability of the weight distribution. We observe that for all models, the kernels with largest weights are estimated robustly (small Fano factor), whereas the kernels with lower weights display more variability (large Fano factor). We also note a qualitative difference between one-dictionary (GM1 and GM2) and two-dictionary (GM3) models. The two-dictionary model has on average fewer kernels (24.58 ± 2.56), with higher mixture weights, resulting in a qualitatively different distribution than the one-dictionary models having on average more kernels (GM1 has 551.68 ± 16.87 kernels and GM2 has 98.60 ± 5.87 kernels) with lower mixture weights.

C. Application: point source localisation

We investigate how the PSF model affects the solution to the PS localisation problem. To assess quantitatively the performance of the different PSF models, we generate synthetic image data using the VM framework [34]. We virtually image a single PS of unit intensity located at a position sampled uniformly within the imaging volume. We vary the exposure time to generate image data at different peak signal-to-noise

ratio (PSNR, adapted from [27]):

$$t_e = \frac{\varphi^{\mathrm{bg}} + \frac{1}{n^{\mathrm{p}}} \sum_{j \in \mathcal{J}} \kappa_{\boldsymbol{\theta}}^{\mathrm{bw}}(\boldsymbol{x}_j - \boldsymbol{x}^{\mathrm{ps}})}{|\mathcal{P}| \max_{j \in \mathcal{J}} \left(\kappa_{\boldsymbol{\theta}}^{\mathrm{bw}}(\boldsymbol{x}_j - \boldsymbol{x}^{\mathrm{ps}}) \right)^2} 10^{0.1\,\mathrm{PSNR}} \ .$$

The image formation parameters are the same as for the SBW dataset (Table I). Sample images are shown in Fig. 8a.

We solve the PS localisation problem using CMA-ES for six PSF models: the ground truth BW; two SG models with parameters estimated either by solving the blind PS deconvolution problem or derived theoretically (SG, SGT, see Section IV-B3); three GM models estimated in Section IV-B4 (GM1, GM2) and Section IV-B6 (GM3). The SG and GM models were calibrated on the SBW data (see Fig. 1a and Table I). It is custom to compare PS localisation algorithms only by the position accuracy. However, we are also interested in the error in intensity. Therefore, we normalise each PSF models such as to match their central mode, which is normalised to one. We summarise the accuracy, the efficiency measures, and the evaluation run-time for each PSF model in Table IV.

We solve independently the PS localisation problem for 100 image stacks. We compute the ℓ_2 error between the ground truth and the estimated values of the PS intensity and position (Fig. 8b). We observe that the lowest errors are achieved by the model matching the ground truth, *i.e.* BW. However, this accuracy comes at a high computational cost (Table IV) due to the repeated computations of integrals (Section II-C1). The SG and SGT approximations result in a nanometer-accurate estimate in position with a low run-time, but at the expense of a higher error in the PS intensity estimate that does not decrease significantly with higher PSNR. Extrapolating the results from Section IV-A, it is likely that the SG model captures both the central mode and the side lobes at the expense of an underestimated central mode amplitude. For SGT, the central mode is better approximated by design [26] and the error in the estimated intensity decreases, up to a certain extent: for higher PSNR, the side lobe contribution becomes significant, and the SGT approximation starts showing its limits.

For each GM model, we solve the PS localisation problem for two cases: when the mixtures are centred around the estimated position of the fluorescent bead during calibration $\widehat{\boldsymbol{x}}^{\mathrm{ps}}$ (see Section III-A6a and Section IV-B3) or centred around the true position $\boldsymbol{x}_{\mathrm{gt}}^{\mathrm{ps}}$, *i.e.* in Section III-B1a we use $\boldsymbol{K}_k(\widehat{\boldsymbol{x}}^{\mathrm{ps}})$

(a) Examples of synthetic images used for point source localisation.

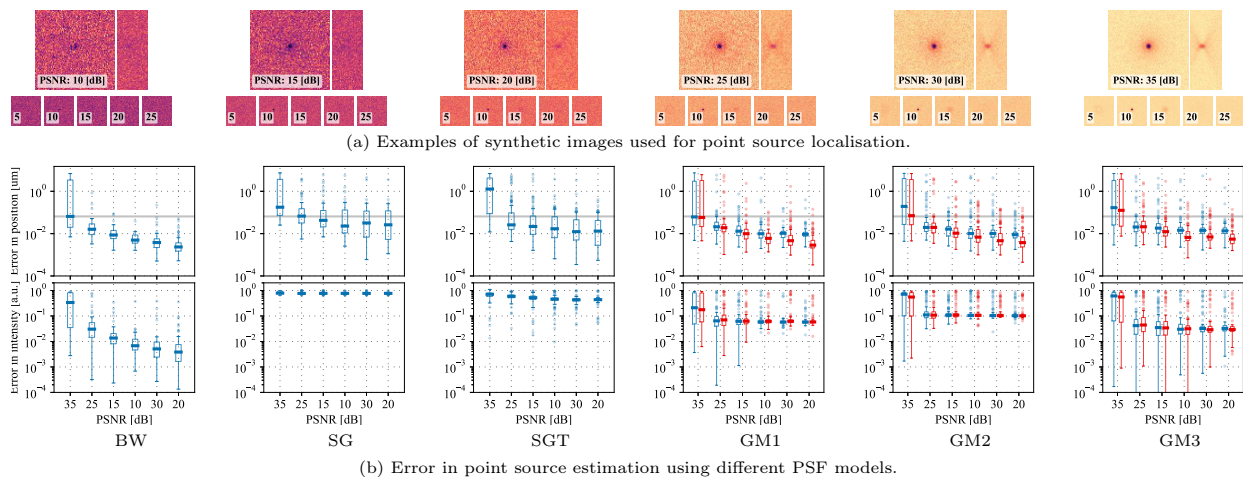(b) Error in point source estimation using different PSF models.

Figure 8. **Comparison of the PSF models in solving the PS localisation problem.** (a) Synthetic image dataset for different PSNR of a PS imaged under a BW PSF model. *First row:* orthogonal z- and x- projections. *Second row:* image slices acquired at different focal planes. (b) Box plots of the ℓ_2 error in PS position (*first row*) and intensity (*second row*) estimated with six PSF models: the ground truth Born and Wolf model (BW); two SG models parametrised by either solving the blind PS deconvolution (SG) or derived from theory (SGT); three GM models (GM1, GM2, GM3) selected on the SBW dataset (see Fig. 6). The horizontal grey line indicates the pixel size. GM models: using $\boldsymbol{K}_k(\widehat{\boldsymbol{x}}^{\mathrm{ps}})$ (blue) or $\boldsymbol{K}_k(\boldsymbol{x}^{\mathrm{ps}}_{\mathrm{gt}})$ (red) in Section III-B1a.

or $\boldsymbol{K}_k(\boldsymbol{x}^{\mathrm{ps}}_{\mathrm{gt}})$, respectively. The former allows quantifying the errors in a real-world scenario, *i.e.* when the PS position used for calibrating the PSF is unknown. The latter allows quantifying the errors in an idealised scenario, *i.e.* when the GM model is optimally calibrated. In the real-world scenario, the GM models result in position estimates with an accuracy comparable with the SG and the SGT models. In the idealised scenario, the accuracy is improved even for GM3, modelled only with 27 Gaussian kernels. In both scenarios, the three GM models result in a significantly lower error in the PS intensity estimate compared with SG and SGT.

V. DISCUSSION

Applying complex PSF models is mainly restricted to digital problems thanks to the efficiency provided by the FFT [45]. However, for inverse problem requiring an analog reconstruction space, such as PS localisation or tracking, complex models become infeasible due to their high evaluation cost. A common solution is to rely on Gaussian approximations [26]. Nonetheless, several approaches have been proposed to enable complex PSF models in applications: speeding up the theoretical models by deriving suitable numerical approximation (*e.g.* approximate complex integrals in the BW model by truncating a Taylor series, see [27]) or by introducing analog phenomenological approximations with a reasonable computational cost (*e.g.* B-Splines and Zernike polynomials). In this work, we propose modelling the PSF using a Gaussian mixture, and we propose a variational framework to achieve an optimal trade-off between reconstruction accuracy and computational efficiency. We believe that we could apply our variational framework to mixtures using other kernels. However, using a Gaussian kernel has the advantage of subsuming the customary Gaussian model and to use a computational back-end with an efficient implementation, *i.e.* the IFGT algorithm [33]. However, we made several simplifying assumptions that lay the ground for future research.

In this paper, we solve the inverse problem for one fluorescent bead, modelled as a point-like object. However, reconstructing the PSF given images of several beads scattered in the image volume can improve the reconstruction accuracy: we expect that such an extension would improve the sparsity of the GM model by filtering out the false positive atoms in the dictionary. It is a straightforward extension that would replace the nll by a sum of nll, one for each bead. This extension lends itself to the operator splitting framework presented in Section III-B1. However, it requires the beads to be identical and the PSF shift invariant. In this work, we modelled a bead using an idealised PS. However, the extended bead size and the asymmetry due to manufacturing imperfections may introduce artefacts in the PSF reconstruction that affect any subsequent inverse problem. A non-point-like fluorescent bead can be modelled using the virtual microscope framework [34]. However, the blind PS deconvolution problem will become more involved. We could potentially explore several extensions: spherical bead with a radius fixed to the value reported by the manufacturer; spherical bead with a radius estimated within a range provided by the manufacturer; or non-spherical bead, requiring shape estimation. Our framework can be extended to space-varying PSFs. In [48], shift-variant PSFs are modelled as a linear combination of shift-invariant PSFs; this is already very close to our representation (10). This extension could be accommodated by our framework by extending the dictionary structure that would account for shift-varying effects.

Our framework applies to both analog and digital dictionaries. However, for simplicity and efficiency, we used a very specific dictionary structure, where each Gaussian kernel is placed at every pixel centre. This allows using a spectral solver based on the FFT for the least-squares problem (see Section III-B1d and Algorithm 1). The advantage is that the large dictionary matrix is not built and hence not stored in memory, providing a good memory footprint to the algorithm [45]. However, our framework can also handle the more general

analog dictionaries, thanks to IFGT, but at the expense of using a spectral solver for the least squares problem. To bypass this limitation, linearising the least-squares problem would result in an explicit step involving only the evaluation of the GM model, amenable to fast computation using IFGT, avoiding to build and store $\mathcal{D}$. We expect that using such analog dictionaries would allow even sparser representation of the GM model. In this paper, we also fix the dictionary structure and kernel parameters. However, one could formulate a more general inverse problem by optimising for both the dictionary and the mixture weights. This would be related to the (non-parametric) dictionary learning problem [49], except, we would restrict the dictionary to a parametric class, *i.e.* Gaussian kernels. This is in contrast to the usual goal of dictionary learning, that is to the best of our knowledge, mostly non-parametric.

To explore the accuracy–efficiency trade-off, we used a convex heuristic based on the ℓ_1 norm to penalise the number of Gaussian kernels. This heuristic entails a bias, that results in our case in biased mixture weights. To alleviate this problem, we use a straightforward refitting strategy that requires only solving a maximum likelihood problem, refitting the weights only for the atoms in the estimated support. However, the need for debiasing stems from the use of a convex heuristic to approximate the non-convex cardinality problem. This non-convex problem could be tackled directly using greedy algorithms such as orthogonal matching pursuit [40]. Another approach would be to use non-convex approximations, or to explore more general sparsity-inducing priors. Both have the advantage of keeping the logic of the operator splitting we presented here. Many well-known sparsity-inducing heuristics can be decomposed as a *difference of convex function*, resulting in an alternating algorithm solving at each iteration a weighted ℓ_1 convex problem [50], [51]. This extension would be straightforward, and our algorithm could be reused as a central component. These methods feature a better sparsity-inducing behaviour, at the expense of non-convex algorithms that require a greater care than their convex counterpart.

VI. Conclusion

Accurate PSF models are fundamental for solving inverse problems in fluorescence microscopy. In practice, Gaussian approximations are favoured for their computational efficiency, at the expense of their ability to capture the rich structures of the PSF tails. In this paper, we introduce a new class of analog PSF models based on a sparse convex combination of Gaussian mixtures (GM). We formulate a maximum *a posteriori* problem for their calibration from image data and derive an efficient algorithm based on a *fully-split formulation* of the *alternating split Bregman* algorithm. Our formulation allows trading accuracy for efficiency by controlling the number of Gaussian mixtures modelling the PSF. We assessed the GM model on synthetic and real image data, and applied it to the point source localisation problem. We showed that the GM model allows a good localisation accuracy together with an improved photometry estimate, at a reasonable computational cost thanks to the IFGT. We believe that our framework will contribute to a wider adoption of more accurate PSF models

and hence improve the reconstruction quality of the intensity signal. This will enable tackling challenging dynamical biological processes from fluorescence microscopy image data.

Appendix
Notations Summary

See Table V at the end of the paper.

References

[1] D. L. Snyder, R. L. White, and A. M. Hammoud, "Image recovery from data acquired with a charge-coupled-device camera." *J. Opt. Soc. Am. A*, vol. 10, no. 5, pp. 1014–1023, 1993.
[2] C. Chesnaud, P. Rélrégier, and V. Boulet, "Statistical region snake-based segmentation adapted to different physical noise models," *IEEE Transactions on Pattern Analysis and Machine Intelligence*, vol. 21, no. 11, pp. 1145–1157, 1999.
[3] G. Paul, J. Cardinale, and I. F. Sbalzarini, "Coupling image restoration and segmentation: A generalized linear model/bregman perspective," *International Journal of Computer Vision*, vol. 104, no. 1, pp. 69–93, 2013.
[4] B. A. Scalettar, J. R. Swedlow, J. W. Sedat, and D. A. Agard, "Dispersion, aberration and deconvolution in multi-wavelength fluorescence images." *Journal of microscopy*, vol. 182, no. Pt 1, pp. 50–60, 1996.
[5] J. G. McNally, T. Karpova, J. Cooper, and J. A. Conchello, "Three-dimensional imaging by deconvolution microscopy." *Methods (San Diego, Calif.)*, vol. 19, no. 3, pp. 373–85, nov 1999.
[6] O. Haeberlé, F. Bicha, C. Simler, A. Dieterlen, C. Xu, B. Colicchio, S. Jacquey, and M.-P. Gramain, "Identification of acquisition parameters from the point spread function of a fluorescence microscope," *Optics communications*, vol. 196, no. September, pp. 109–117, 2001.
[7] P. Pankajakshan, B. Zhang, L. Blanc-Féraud, Z. Kam, J.-C. Olivo-Marin, and J. Zerubia, "Blind deconvolution for thin-layered confocal imaging." *Applied optics*, vol. 48, no. 22, pp. 4437–4448, 2009.
[8] S. B. Hadj, L. Blanc-Féraud, G. Aubert, and G. Engler, "Blind restoration of confocal microscopy images in presence of a depth-variant blur and Poisson noise," *IEEE International Conference on Acoustics, Speech and Signal Processing (ICASSP)*, pp. 915–919, 2013.
[9] M. Born and E. Wolf, *Principles of optics*. CUP Archive, 2000.
[10] S. F. Gibson and F. Lanni, "Experimental test of an analytical model of aberration in an oil-immersion objective lens used in three-dimensional light microscopy," *Journal of the Optical Society of America A*, vol. 9, no. 1, p. 154, 1992.
[11] S. Hell, G. Reiner, C. Cremer, and E. H. K. Stelzer, "Aberrations in confocal fluorescence microscopy induced by mismatches in refractive index," *Journal of microscopy*, vol. 169, no. 3, pp. 391–405, 1993.
[12] P. Török and P. Varga, "Electromagnetic diffraction of light focused through a stratified medium." *Applied optics*, vol. 36, no. 11, pp. 2305–2312, 1997.
[13] O. Haeberlé, "Focusing of light through a stratified medium: A practical approach for computing microscope point spread functions: Part II: Confocal and multiphoton microscopy," *Optics Communications*, vol. 235, no. 1-3, pp. 1–10, 2002.
[14] S. Ghosh and C. Preza, "Fluorescence microscopy point spread function model accounting for aberrations due to refractive index variability within a specimen," *Journal of Biomedical Optics*, vol. 20, no. 7, p. 075003, 2015.
[15] J.-B. Sibarita, "Deconvolution Microscopy," *Microscopy Techniques*, pp. 201–243, 2005.
[16] D. Agard, Y. Hiraoka, P. Shaw, and J. Sedat, "Fluorescence Microscopy in Three Dimensions," *Methods in cell biology*, vol. 30, pp. 353–377, 1989.
[17] Y. Hiraoka, J. W. Sedat, and D. A. Agard, "Determination of three-dimensional imaging properties of a light microscope system. Partial confocal behavior in epifluorescence microscopy." *Biophysical journal*, vol. 57, no. 2, pp. 325–33, 1990.

[18] P. J. Shaw and D. J. Rawlings, "The point-spread function of a confocal microscope: its measurement and use in deconvolution of 3–D data," *Journal of Microscopy*, vol. 163, no. October 1990, pp. 151–165, 1991.

[19] J. Boutet de Monvel, S. Le Calvez, and M. Ulfendahl, "Image Restoration for Confocal Microscopy: Improving the Limits of Deconvolution, with Application to the Visualization of the Mammalian Hearing Organ," *Biophysical Journal*, vol. 80, no. 5, pp. 2455–2470, 2001.

[20] R. Juškaitis, *Measuring the Real Point Spread Function of High Numerical Aperture Microscope Objective Lenses*. Boston, MA: Springer US, 2006, pp. 239–250. [Online]. Available: https://doi.org/10.1007/978-0-387-45524-2_11

[21] J. Boutet De Monvel, E. Scarfone, S. Le Calvez, and M. Ulfendahl, "Image-Adaptive Deconvolution for Three-Dimensional Deep Biological Imaging," *Biophysical Journal*, vol. 85, no. 6, pp. 3991–4001, 2003.

[22] J. W. Shaevitz and D. A. Fletcher, "Enhanced three-dimensional deconvolution microscopy using a measured depth-varying point-spread function." *Journal of the Optical Society of America A. Optics, image science, Hanser2004and vision*, vol. 24, no. 9, pp. 2622–2627, 2007.

[23] J. G. McNally, C. Preza, J. A. Conchello, and L. J. Thomas, "Artifacts in computational optical-sectioning microscopy." *Journal of the Optical Society of America A. Optics, image science, and vision*, vol. 11, no. 3, pp. 1056–1067, 1994.

[24] P. Pankajakshan, L. Blanc-Féraud, Z. Kam, and J. Zerubia, "Point-spread function retrieval for fluorescence microscopy," *IEEE International Symposium on Biomedical Imaging (ISBI)*, pp. 1095–1098, 2009.

[25] B. M. Hanser, M. G. Gustafsson, D. A. Agard, and J. W. Sedat, "Phase-retrieved pupil functions in wide-field fluorescence," *Journal of Microscopy*, vol. 216, pp. 32–48, 2004.

[26] B. Zhang, J. Zerubia, and J. Olivo-Marin, "Gaussian approximations of fluorescence microscope point-spread function models," *Applied Optics*, vol. 46, no. 10, pp. 1819–1829, 2007.

[27] F. Aguet, "Super-resolution fluorescence microscopy based on physical models," Ph.D. dissertation, École Polytechnique Fédérale de Lausanne (EPFL), School of Engineering, 2009.

[28] A. Small and S. Stahlheber, "Fluorophore localization algorithms for super-resolution microscopy," *Nature Methods*, vol. 11, no. 3, pp. 267–279, 2014.

[29] N. Bissantz, H. Holzmann, and M. Pawlak, "Improving PSF calibration in confocal microscopic imaging-estimating and exploiting bilateral symmetry," *Annals of Applied Statistics*, vol. 4, no. 4, pp. 1871–1891, 2010.

[30] E. Maalouf, B. Colicchio, and A. Dieterlen, "Fluorescence microscopy three-dimensional depth variant point spread function interpolation using Zernike moments," *Journal of the Optical Society of America A*, vol. 28, no. 9, p. 1864, 2011.

[31] H. Kirshner, C. Vonesch, and M. Unser, "Can localization microscopy benefit from approximation theory?" *IEEE International Symposium on Biomedical Imaging (ISBI)*, pp. 584—-587, 2013.

[32] A. Tahmasbi, E. S. Ward, and R. J. Ober, "Determination of localization accuracy based on experimentally acquired image sets: applications to single molecule microscopy," *Opt. Express*, vol. 23, no. 6, pp. 7630–7652, 2015.

[33] C. Yang, R. Duraiswami, N. A. Gumerov, and L. Davis, "Improved fast gauss transform and efficient kernel density estimation," *IEEE International Conference on Computer Vision*, pp. 664–671, 2003.

[34] D. K. Samuylov, L. A. Widmer, G. Szekely, and G. Paul, "Mapping complex spatio-temporal models to image space: The virtual microscope," *IEEE International Symposium on Biomedical Imaging (ISBI)*, pp. 707–711, 2015.

[35] M. Hirsch, R. J. Wareham, M. L. Martin-Fernandez, M. P. Hobson, and D. J. Rolfe, "A Stochastic Model for Electron Multiplication Charge-Coupled Devices – From Theory to Practice," *PLoS ONE*, vol. 8, no. 1, p. e53671, 2013.

[36] M. Konnik and J. Welsh, "High-level numerical simulations of noise in CCD and CMOS photosensors: review and tutorial," *arXiv:1412.4031*, pp. 1–21, 2014.

[37] W. Richardson, "Bayesian-based iterative method of image restoration," *Journal of the Optical Society of America*, vol. 62, no. I, pp. 55–59, 1972.

[38] É. Thiébaut, L. Denis, F. Soulez, and R. Mourya, "Spatially variant PSF modeling and image deblurring," in *Proceedings of SPIE*, vol. 9909, no. 2, 2016, p. 99097N.

[39] V. I. Morariu, B. V. Srinivasan, V. C. Raykar, R. Duraiswami, and L. S. Davis, "Automatic online tuning for fast Gaussian summation," *Transform*, pp. 1–8, 2008.

[40] F. Bach, R. Jenatton, J. Mairal, and G. Obozinski, "Optimization with Sparsity-Inducing Penalties," *Foundations and Trends® in Machine Learning*, vol. 4, no. 1, pp. 1–106, 2012.

[41] C.-A. Deledalle, N. Papadakis, and J. Salmon, "On debiasing restoration algorithms: Applications to total-variation and nonlocal-means," in *Scale Space and Variational Methods in Computer Vision*, J.-F. Aujol, M. Nikolova, and N. Papadakis, Eds. Cham: Springer International Publishing, 2015, pp. 129–141.

[42] S. Setzer, G. Steidl, and T. Teuber, "Deblurring Poissonian images by split Bregman techniques," *Journal of Visual Communication and Image Representation*, vol. 21, no. 3, pp. 193–199, 2010.

[43] N. Hansen, S. D. Müller, and P. Koumoustakos, "Reducing the time complexity of the derandomizes evolution strategy with covariance matrix adaptation (CMA-ES)," *Evolutionary Computation*, vol. 11, no. 1, pp. 1–18, 2003.

[44] G. Strang, "The Discrete Cosine Transform," *Socitey of Industrial and Applied Mathematics*, vol. 41, no. 1, pp. 135–147, 1999.

[45] P. Hansen, J. Nagy, and D. O'Leary, *Deblurring Images*. Society for Industrial and Applied Mathematics, 2006.

[46] R. J. Hyndman, "Computing and Graphing Highest Density Regions," *The American Statistician*, vol. 50, no. 2, pp. 120–126, 1996.

[47] H. Kirshner, D. Sage, and M. Unser, "3D PSF models for fluorescence microscopy in ImageJ," in *Proceedings of the Twelfth International Conference on Methods and Applications of Fluorescence Spectroscopy, Imaging and Probes (MAF'11)*, Strasbourg, French Republic, September 11-14, 2011, p. 154.

[48] L. Denis, E. Thiébaut, F. Soulez, J. M. Becker, and R. Mourya, "Fast Approximations of Shift-Variant Blur," *International Journal of Computer Vision*, vol. 115, no. 3, pp. 253–278, 2015.

[49] J. Mairal, F. Bach, and J. Ponce, "Sparse modeling for image and vision processing," *Foundations and Trends® in Computer Graphics and Vision*, vol. 8, no. 2-3, pp. 85–283, 2014. [Online]. Available: http://dx.doi.org/10.1561/0600000058

[50] G. Gasso, A. Rakotomamonjy, and S. Canu, "Recovering sparse signals with a certain family of nonconvex penalties and DC programming," *IEEE Transactions on Signal Processing*, vol. 57, no. 12, pp. 4686–4698, 2009.

[51] H. A. Le Thi, T. Pham Dinh, H. M. Le, and X. T. Vo, "DC approximation approaches for sparse optimization," *European Journal of Operational Research*, vol. 244, no. 1, pp. 26–46, 2015.

Denis K. Samuylov received the B.Sc. degree in telecommunications from the Saint Petersburg State Polytechnic University (currently the Peter the Great Saint Petersburg Polytechnic University), Russia, in 2011. He received the M.Sc. degree in interdisciplinary approaches to life science from the Paris Diderot University (Paris 7), France, in 2013. He received the Ph.D. degree in computer vision from the Computer Vision laboratory at the Swiss Federal Institute of Technology in Zurich (ETH Zurich), Switzerland, in 2018. His research interests include the application of signal processing and computer vision techniques to various problems in biology and medicine.

Prateek Purwar Prateek Purwar received the B.Tech. degree in Electrical Engineering from Indian Institute of Technology Bombay, Mumbai, India in 2009. He received the M.Sc. degree in Electrical Engineering from Swiss Federal Institute of Technology in Zurich (ETH Zurich), Switzerland, in 2017. His research interests mainly include the application of signal processing, machine learning and computer vision techniques for solving various problems in medicine and automation industry.

Gábor Székely received the Graduate degree in chemical engineering, the Graduate degree in applied mathematics, and the Ph.D. degree in analytical chemistry from the Technical University of Budapest and the Eötvös Lórand University, Budapest, Hungary, in 1974, 1981, and 1985, respectively. Since 2002 he has been leading the Medical Image Analysis and Visualization Group at the Computer Vision Laboratory of Swiss Federal Institute of Technology (ETH) Zurich, Switzerland, concentrating on the development of image analysis, visualization, and simulation methods for computer support of biomedical research, clinical diagnosis, therapy, training and education.

Grégory Paul received the M.Sc. degree in cell biology and physiology from Ecole Normale Supérieure, Paris, France, in 2003, and the Ph.D. degree from the University of Paris VI, in 2008. In 2008 he joined the Swiss Federal Institute of Technology (ETH) Zurich, Switzerland, as a post-doctoral researcher in the computer science department with Prof. Ivo F. Sbalzarini to develop new quantitative tools to investigate biological processes from image data. Together with Prof. Gábor Székely, between 2012 and 2017 he was leading the BioimagE Analysis and Modeling (BEAM) team, at ETH in the Computer Vision Laboratory, focusing on the development of image analysis, computational statistics and biophysical modeling applied to cell biology.

Table V
SUMMARY OF NOTATIONS USED IN THE PAPER

Notation	Description
$\boldsymbol{x} := (x,y,z) \in \mathbb{R}^3$	Arbitrary point in physical space
$\boldsymbol{x}^{\mathrm{ps}} \in \mathbb{R}^3$	Position of a point source
$\varphi^{\mathrm{ps}} \in \mathbb{R}_+$	Photon emission rate of a point source
$\varphi^{\mathrm{bg}} \in \mathbb{R}_+$	Photon emission rate of the background
$\mathrm{d}\boldsymbol{x}$	Lebesgue measure in space
$\mathrm{d}t$	Lebesgue measure in time
$\delta_{\boldsymbol{x}}(\mathrm{d}\boldsymbol{x})$	Dirac measure positioned at $\boldsymbol{x}$
$\phi^{\mathrm{obj}}(\mathrm{d}\boldsymbol{y} \times \mathrm{d}t)$	Spatio-temporal object measure modelling the total photon flux emitted by a point source object and the background
t_e	Exposure time
$\Omega \subset \mathbb{R}^3$	Imaging volume
$|\mathcal{P}|$	Pixel area
Δ_{xy}	Pixel size
$n^{\mathrm{h}} \times n^{\mathrm{w}}$	Camera detector size (in pixels)
Δ_z	Distance between two focal planes
n^{s}	Number of focal planes
$\boldsymbol{Z} \in \mathbb{Z}_+^{n^{\mathrm{s}} \times n^{\mathrm{h}} \times n^{\mathrm{w}}}$	Image stack data (grey values)
$\mathcal{J} := \{1, \ldots, n^{\mathrm{p}}\}$	Linear indices over $\boldsymbol{Z}$, with $n^{\mathrm{p}} := n^{\mathrm{s}}n^{\mathrm{h}}n^{\mathrm{w}}$
$\mathcal{P}_j \subset \Omega$	Surface of the j-th pixel in physical space
$\boldsymbol{x}_j \in \Omega$	Centre of the j-th pixel in physical space
$\mu_j(\phi)$	Expected photon count at the j-th pixel
N_j^{photon}	(Random) photon count at the j-th pixel
N_j^{grey}	(Random) grey value at the j-th pixel
ν see eq. (6)	Pixel-to-image mapping modelling the conversion of photons hitting the detector surface N_j^{photon} into grey values N_j^{grey}
λ	emission wave length
q_λ	quantum efficiency at λ
M	multiplication gain
f	analog-to-digital proportionality factor
b	camera bias
NA	Numerical aperture
n_i	Refractive index of the immersion medium
$\kappa(\mathrm{d}\boldsymbol{x} \mid \boldsymbol{y})$	Transition probability kernel
$\kappa_{\boldsymbol{\theta}}(\boldsymbol{y})$	PSF kernel with parameters $\boldsymbol{\theta} \in \boldsymbol{\Theta}$
$\boldsymbol{\theta}^{\mathrm{bw}} := \{\lambda, \mathrm{NA}, n_i\}$	Parameters of the Born and Wolf model
$\boldsymbol{\theta}^{\mathrm{sg}} := \{\sigma_{xy}, \sigma_z\}$	Lateral and axial standard deviations parametrising single Gaussian PSF models
$\Sigma_{\boldsymbol{\theta}} \in \mathbb{R}^{3 \times 3}$	Covariance matrix of a Gaussian kernel
$\mathcal{D}$	Parametric dictionary describing Gaussian mixture (GM) PSF model, where each atom is a shifted SG kernel
$|\mathcal{D}|$	Dictionary size, *i.e.* the number of Gaussian kernels in the mixture
$\boldsymbol{\theta}^{\mathcal{D}}$	Parameters of the kernels in $\mathcal{D}$
$\mathcal{K} := \{1, \ldots, n^{\mathcal{C}}\}$	Index set of the covariance matrices in $\mathcal{D}$
$\mathcal{X}_k$ with $k \in \mathcal{K}$	Set of $n_k^{\mathcal{X}}$ positions in $\mathcal{D}$ associated with a Gaussian kernel parameterised by $\boldsymbol{\theta}_k^{\mathrm{sg}}$
$\mathcal{M}_k := \{1, \ldots, n_k^{\mathcal{X}}\}$	Indices over $\mathcal{X}_k$

Notation	Description
$\Delta_{|\mathcal{D}|}$	Probability simplex defined as the convex hull of the $|\mathcal{D}| + 1$ standard unit vectors
$\boldsymbol{v} \in \Delta_{|\mathcal{D}|}$	Vector of mixture weights v_{km} with $k \in \mathcal{K}$ and $m \in \mathcal{M}_k$
$\boldsymbol{v}_k \in \mathbb{R}_+^{n_k^{\mathcal{X}}}$	Vector obtain by grouping the weights associated with a Gaussian mixture parameterised by $\boldsymbol{\theta}_k$: $[\boldsymbol{v}_k]_m := v_{km}$
$\boldsymbol{\varphi}_k^{\mathrm{net}} \in \mathbb{R}_+^{n_k^{\mathcal{X}}}$	Net mixture intensity defined as $\varphi^{\mathrm{ps}}\boldsymbol{v}_k$
$\boldsymbol{\varphi}^{\mathrm{net}} \in \mathbb{R}_+^{|\mathcal{D}|}$	Stacked vector of net mixture intensities
$\mathrm{supp}(\boldsymbol{v})$	Support of the mixture weights defined as a set of indices of non-zero mixture weights
$\boldsymbol{\theta}^{\mathrm{gm}} := \boldsymbol{\theta}^{\mathcal{D}} \cup \{\boldsymbol{v}\}$	Parameters of the Gaussian mixture model
nll	Data fitting term defined as a normalised negative log-likelihood, also called in statistics deviance or Bregman divergence, see [3]
$\mathrm{nll}_{\mathrm{p}}$	nll scaled by n^{p}
R	Regularisation term (prior about the model parameters)
η	Regularisation parameter controlling the trade-off between nll and R
$\boldsymbol{\eta} \in \mathbb{R}_+^{n^{\mathcal{C}}}$	Vector of $n^{\mathcal{C}}$ regularisation parameters associated with a set of kernels parameterised by $\boldsymbol{\theta}_k^{\mathrm{sg}}$
$\boldsymbol{n} \in \mathbb{R}_+^{n^{\mathrm{p}}}$	Vectorised raw photon counts obtained by applying the inverse of ν to $\boldsymbol{Z}$
$\boldsymbol{\mu} \in \mathbb{R}_+^{n^{\mathrm{p}}}$	Vector of expected photon counts computed according to object-to-pixel mapping at each pixel $j \in \mathcal{J}$
$\boldsymbol{\kappa}_k(\boldsymbol{x}) \in \mathbb{R}_+^{n_k^{\mathcal{X}}}$	Vector obtained by evaluating a Gaussian mixture parameterised by $\boldsymbol{\theta}_k$ at $\boldsymbol{x} - \boldsymbol{x}_{km}$ with $\boldsymbol{x}_{km} \in \mathcal{X}_k$
$\boldsymbol{K}_k(\boldsymbol{x}) \in \mathbb{R}_+^{n^{\mathrm{p}} \times n_k^{\mathcal{X}}}$	Blurring matrix where each row is defined as $\boldsymbol{\kappa}_k(\boldsymbol{x}_j - \boldsymbol{x})$ at each pixel $j \in \mathcal{J}$
$\boldsymbol{0}_n \in \mathbb{R}^n$	n-dimensional vector of zeros
$\boldsymbol{1}_n \in \mathbb{R}^n$	n-dimensional vector of ones
$\boldsymbol{I}_n \in \mathbb{R}^{n \times n}$	Identity matrix
$\iota_{\mathcal{S}}(\boldsymbol{\varphi})$	Indicator functional that assumes 0 if $\boldsymbol{\varphi}$ is componentwise non-negative and $+\infty$ otherwise